

The Parkes Galactic Meridian Survey (PGMS): observations and CMB polarization foreground analysis

E. Carretti,^{1,2*} M. Haverkorn,^{3,4,5} D. McConnell,² G. Bernardi,⁶
N.M. McClure-Griffiths,² S. Cortiglioni,⁷ and S. Poppi,⁸

¹INAF, Istituto di Radioastronomia, Via Gobetti 101, I-40129 Bologna, Italy

²CSIRO, Australia Telescope National Facility, P.O. Box 76, Epping, NSW 1710, Australia

³Jansky Fellow, National Radio Astronomy Observatory

⁴Astronomy Department, University of California, Berkeley, 601 Campbell Hall, Berkeley, CA 94720

⁵ASTRON, Oude Hoogeveensedijk 4, 7991 PD Dwingeloo, The Netherlands

⁶Kapteyn Astronomical Institute, University of Groningen, P.O. Box 800, 9700 AV Groningen, the Netherlands

⁷INAF, Istituto di Astrofisica Spaziale e Fisica Cosmica Bologna, Via Gobetti 101, 40129 Bologna, Italy

⁸INAF, Osservatorio Astronomico di Cagliari, Loc. Poggio dei Pini, Strada 54, 09012 Capoterra, Italy

Accepted xxxx. Received yyyy; in original form zzzz

ABSTRACT

We present observations, maps, polarised emission properties study, and CMB foreground analysis of the Parkes Galactic Meridian Survey (PGMS), a project to investigate the Galactic latitude behaviour of the polarized synchrotron emission at 2.3 GHz with the Parkes Radio Telescope. The survey consists of a 5° wide strip along the Galactic meridian $l = 254^\circ$ extending from the Galactic plane to the South Galactic pole. We identify three zones distinguished by polarized emission properties: the disc, the halo, and a transition region connecting them. The halo section lies at latitudes $|b| > 40^\circ$ and is characterised by weak and smooth polarized emission with most of the power on large scale and steep angular power spectra of median slope $\beta_{\text{med}} \sim -2.6$. The disc region covers the latitudes $|b| < 20^\circ$ and shows a brighter, more complex emission dominated by the small scales with inverted spectra of mean slope $\bar{\beta} = -1.8$. The transition region has steep spectra as in the halo, but the emission power increases toward the Galactic plane from halo to disc levels. The change of slope and emission structure at $b \sim -20^\circ$ is sudden, indicating a sharp disc-halo transition. The whole halo section is just one environment extended over 50° with very low emission which, once scaled to 70 GHz, is equivalent to the CMB emission for a tensor-to-scalar perturbation power ratio $r_{\text{halo}} = (3.3 \pm 0.4) \times 10^{-3}$. Applying a conservative cleaning procedure, we estimate an r detection limit of $\delta r \sim 7 \times 10^{-3}$ at 150 GHz and $\delta r \sim 2 \times 10^{-3}$ at 70 GHz (3-sigma C.L.). Our results have implications for the optimal strategies for measuring the B -mode. The limit at 150 GHz is better than the goals of the planned suborbital experiments, which can therefore be conducted at this high frequency with benefits from a more compact size. The limit at 70 GHz is close to the goal of the proposed next generation space missions ($r \sim 1 \times 10^{-3}$), which thus might not strictly require to go to space. The space option might be left to probe down to the ultimate values accessible by the CMB ($r \sim 10^{-5}$), which require an all-sky survey. The survey data will be made available at the site <http://www.atnf.csiro.au/people/Ettore.Carretti/PGMS>

Key words: Cosmology: CMB – Galaxy: disk – Galaxy: halo – polarization

1 INTRODUCTION

The study of the polarized synchrotron emission is essential for two cutting-edge fields of the current astrophysics

research: the detection of the B -Mode of the Cosmic Microwave Background (CMB), for which the Galactic synchrotron is a foreground emission, and the investigation of the large scale magnetic field of the Galaxy.

The CMB B -mode is a direct signature of the primordial gravitational wave background (GWB) left

* E-mail: Ettore.Carretti@csiro.au (EC)

by the inflation (e.g., Kamionkowski & Kosowsky 1998; Boyle, Steinhardt, & Turok 2006). The amplitude of its angular power spectrum is proportional to the GWB power and is measured by the tensor-to-scalar perturbation power ratio r . Still undetected, the current upper limit is set to $r < 0.20$ (95% C.L., Komatsu et al. 2009) by the 5-yr results of the Wilkinson Microwave Anisotropy Probe (WMAP). Besides the evidence of a primordial GWB a measure of r would help distinguish among several inflation models and investigate the physics of the early stages of the Universe.

However, this spectacular science goal is made difficult by the CMB B -Mode tiny signal, which ranges from about $0.1 \mu\text{K}$ of the present upper limit down to 1 nK of the smallest r accessible by CMB ($r \sim 10^{-5}$, Amarie, Hirata & Seljak 2005). Besides the challenge of the required sensitivity, at such low levels the cosmic signal is easily overcome by the Galactic foreground of the synchrotron and dust emissions, which can set the actual detection limit.

Investigations of the synchrotron contribution have been conducted in the last years, but data are still insufficient to give a comprehensive view (Fig. 1). Page et al. (2007) analyse the 23 GHz WMAP polarized maps and find that the normal emission at high Galactic latitude is strong: at 70 GHz it is *equivalent to*¹ $r \sim 0.3$, which is even higher than the current upper limit. Some small areas have been observed in selected low emission regions and feature more hopeful conditions, with the synchrotron contribution at 70 GHz equivalent to $r = [3 \times 10^{-3}, 1 \times 10^{-2}]$ (see

Carretti, Bernardi & Cortiglioni 2006b for a review). However, these areas cover a few square degrees and it is not clear whether they are particularly good, but rare, spots or representative of the normal conditions of the low emission regions. A first analysis to understand position, extension, and properties of the best regions shows that they cover a significant part of the sky (about 15%, Carretti et al. 2006b). However, the emission level is still poorly constrained ranging in $r = [1 \times 10^{-3}, 1 \times 10^{-2}]$, limited by the sensitivity of the available data (WMAP maps). Finally, some extended high Galactic latitude areas have been investigated at 1.4 GHz and feature a synchrotron contribution equivalent to $r \sim 7 \times 10^{-2}$ (at 70 GHz, La Porta et al. 2006). However, these have not been selected among the best sky areas.

The current picture is therefore that the synchrotron contamination is strong at high Galactic latitudes with a typical emission even higher than the current upper limit of the CMB B -Mode. This requires an aggressive foreground cleaning to search for the inflation signature with all-sky class surveys. Better conditions seem to exist in 15% of the sky, but the present data are not sufficient to set the detection limit of r . This point is crucial especially for ground-based and balloon-borne experiments, which are devised to observe in small sky areas.

Another important open point is the frequency of minimum foreground emission because of its implications for the experiment design. WMAP finds that this is in the range 60–70 GHz for high Galactic latitudes (Page et al. 2007), but it is still an unanswered question in the best part of the

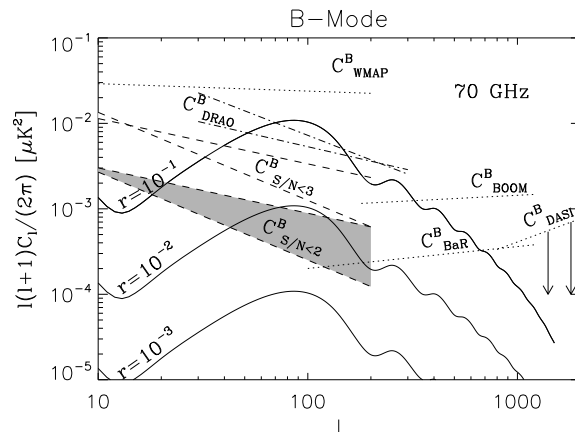


Figure 1. Status of the knowledge about the B -Mode power spectra of the Galactic synchrotron emission as for before this paper. Spectra are estimated at 70 GHz. A brightness temperature frequency slope of $\alpha = -3.1$ has been assumed for all extrapolations. C_{WMAP}^B is the general contamination at high Galactic latitude, as estimated by the WMAP team using a $\sim 75\%$ sky fraction at 22.8-GHz (Page et al. 2007). The spectra measured in small areas selected for their low emission are also reported: the target fields of the experiments BOOMERanG (C_{BOOM}^B , Carretti et al. 2005b) and BaR-SPOrt (C_{BaR}^B , Carretti et al. 2006a), and the upper limit found in the two fields of the experiment DASI (C_{DASI}^B , Bernardi et al. 2006). Finally, $C_{S/N<2}$ shows the estimate of the emission in the best 15% of the sky (Carretti et al. 2006b, the shaded area indicates the uncertainties), while C_{DRAO} the values found in some intermediate regions using 1.4 GHz data (La Porta et al. 2006). For comparison, CMB spectra for three different values of r are also shown.

sky. It has been speculated that the dust emission should have minima deeper than the synchrotron in lowest emission areas (e.g., Lange 2008), so that the best window could shift to higher frequencies. However, the synchrotron contribution is usually estimated from the WMAP data, which are noise dominated at high latitudes leading to possible overestimates.

The study of the magnetic field in the disc of our Galaxy has made significant advances in the last few years. Observations of external spiral galaxies show that the spiral arms are usually dominated by a turbulent or tangled component with a weaker coherent large scale field aligned with the arms. In the inter-arm regions the regular component is more relevant and depicts magnetic arms with coherent scales up to the size of the disc (e.g. see Beck 2008 for a review).

Although the case of our Galaxy is harder to understand because of our internal location, recent high sensitivity and high spatial density Rotation Measure (RM) data has enabled the first studies of the 3D structure in the disc (e.g. Han et al. 2006; Haverkorn et al. 2006; Brown et al. 2007). What seems most favoured is a spiral structure down to the inner disc edge, where the field might take on a ring shape (e.g. Brown et al. 2007; Sun et al. 2008). The field in the local arm is clock-wise as seen from the north Galactic pole, while at least one reversal (inversion of the field direction while keeping the same alignment) seems to take place toward the inner Galaxy. Even though a general consensus

¹ With “*equivalent to* r ” we intend the r value for which the CMB B -Mode spectrum matches that of the foreground.

on the basis of this framework seems to have taken place, crucial points to distinguish among several models are still under debate, like the number and location of the reversals and the existence of the ring.

The field structure of the halo is less clear. This is not only because it is harder to detect the synchrotron emission in this low emission region, but also because of the many different patterns observed in external galaxies: from galaxies without evident halo field, to X-shaped fields centred at the galaxy centre, and up to large almost spherical magnetic halos (see Beck 2008 for a review). For our Galaxy, data are far less abundant than those in the disc and models are essentially unconstrained. Our knowledge is based on RMs of extragalactic sources and pulsars at mid and high Galactic latitudes, which are coarsely and irregularly sampled. Han (2002) finds that RM values are asymmetric both with respect to the plane and the Galactic centre in the inner Galaxy, which is compatible with a field generated by an α - Ω dynamo model of A0-mode: two toroidal fields above and under the Galactic plane antisymmetric across the plane (sign reversal). However, diffuse polarization maps at 1.4 and 22.8 GHz (Wolleben et al. 2006; Testori et al. 2008; Page et al. 2007) clearly show very large structures in that region extending from the plane up to high latitudes. These likely are of very local origin, and contamination of RM data by local anomalies is possible. Recently, Sun et al. (2008) have used most of the available data but find that their model cannot yet constrain the halo field because of lack of data. Therefore, more data are necessary to understand how the field in the Galactic halo is structured.

More systematic observations of the synchrotron polarized emission are thus necessary, at all Galactic latitudes, both to explore the behaviour of the contamination of the CMB with the latitude and to study the Galactic magnetic field in the disc, halo, and at the disc-halo transition.

All-sky polarization data are available at 1.4 GHz and 23 GHz. However, the 1.4 GHz maps show that the disc emission is strongly depolarized up to latitudes $|b| \sim 30^\circ$ (Wolleben et al. 2006; Testori et al. 2008), while Faraday Rotation (FR) effects are still present up to $|b| \sim 40^\circ$ – 50° (Carretti et al. 2005a). Furthermore, those data are single frequency and do not enable RM computations. The WMAP data at 23 GHz are virtually unaffected by FR effects, but the sensitivity is not sufficient since, once binned in 2° pixels, about 55% of the sky features a $S/N < 3$. This area corresponds to all the high Galactic latitudes with the exception of large local structures, which is most of the sky useful both for CMB aims and to study the large scale magnetic field.

Therefore, the available polarized synchrotron emission surveys are insufficient and data at intermediate frequencies are needed.

In this work we present the Parkes Galactic Meridian Survey (PGMS), a survey conducted with the Parkes Radio Telescope to cover a strip along an entire southern Galactic meridian at 2.3 GHz. The area is free from large local structures, making it ideal for investigating both the CMB foregrounds and the Galactic magnetic field. The PGMS overlaps the target area of several CMB experiments like BOOMERanG (Masi et al. 2006), QUAD (Pryke et al. 2008), BICEP (Takahashi et al. 2008), EBEX (Grainger et al. 2008), and CLOVER (North et al. 2008).

Our results may have direct implications for all these experiments.

In this paper we present the survey, observations, and a characterisation of the polarized emission. We also present an analysis of the measured emission as a contaminating foreground to CMB B -mode emission. Analysis and implications for the Galactic magnetic field will be subject of a forthcoming paper (Paper II, Haverkorn et al. 2009 in preparation). A third paper will deal with the polarized extragalactic sources (paper III, Bernardi et al. 2009 in preparation).

Survey and observations are presented in Sect. 2, the ground emission analysis in Sect. 3, and the maps in Sect. 4. The analysis of both the angular power spectrum and emission behaviour is presented in Sect. 5, while the dust contribution is investigated in Sect. 6. The detection limits of r are discussed in Sect. 7 and, finally, our summary and conclusions are reported in Sect. 8.

2 THE PARKES GALACTIC MERIDIAN SURVEY

The available data and the properties of the synchrotron emission discussed in Sect. 1 lead to the following main requirements for a survey. Observations must

- (i) be conducted at a low enough radio frequency for the synchrotron emission to dominate the other diffuse emission components, but at a frequency higher than 1.4 GHz to avoid significant Faraday Rotation effects;
- (ii) have sufficient frequency resolution to enable rotation measure computation;
- (iii) cover all latitudes from the Galactic plane to the pole, to explore the behaviour with the Galactic latitude b ;
- (iv) cover regions free from large local structures, such as the big radio loops, that would distort the estimates of normal conditions at high latitudes.

The Parkes Galactic Meridian Survey (PGMS) is a project to survey the diffuse polarized emission along a Galactic meridian designed to satisfy these requirements. It surveys a $5^\circ \times 90^\circ$ strip 5° wide along the entire southern meridian $l = 254^\circ$ from the Galactic plane to the south Galactic pole (Fig. 2). The observations have been carried out at 2.3 GHz with the Parkes Radio Telescope (NSW, Australia), a facility operated by the Australia Telescope National Facility² (ATNF) a division of CSIRO³. It also includes an $10^\circ \times 10^\circ$ extension centred at $l = 251^\circ$ and $b = -35^\circ$.

The selected meridian goes through one of the low emission regions of the sky as identified using the WMAP data (Fig. 2, see also Carretti et al. 2006b) and is free of large local emission structures. The meridian also goes through the area of deep polarization observations of the BOOMERanG experiment (Masi et al. 2006) and the 10° extension near $b = -35$ degrees is positioned to best cover that.

The synchrotron emission is best studied at low frequencies because of its steep negative spectral index, whereas

² <http://www.atnf.csiro.au>

³ <http://www.csiro.au>

PGMS area + 22.8 GHz Polarized Intensity

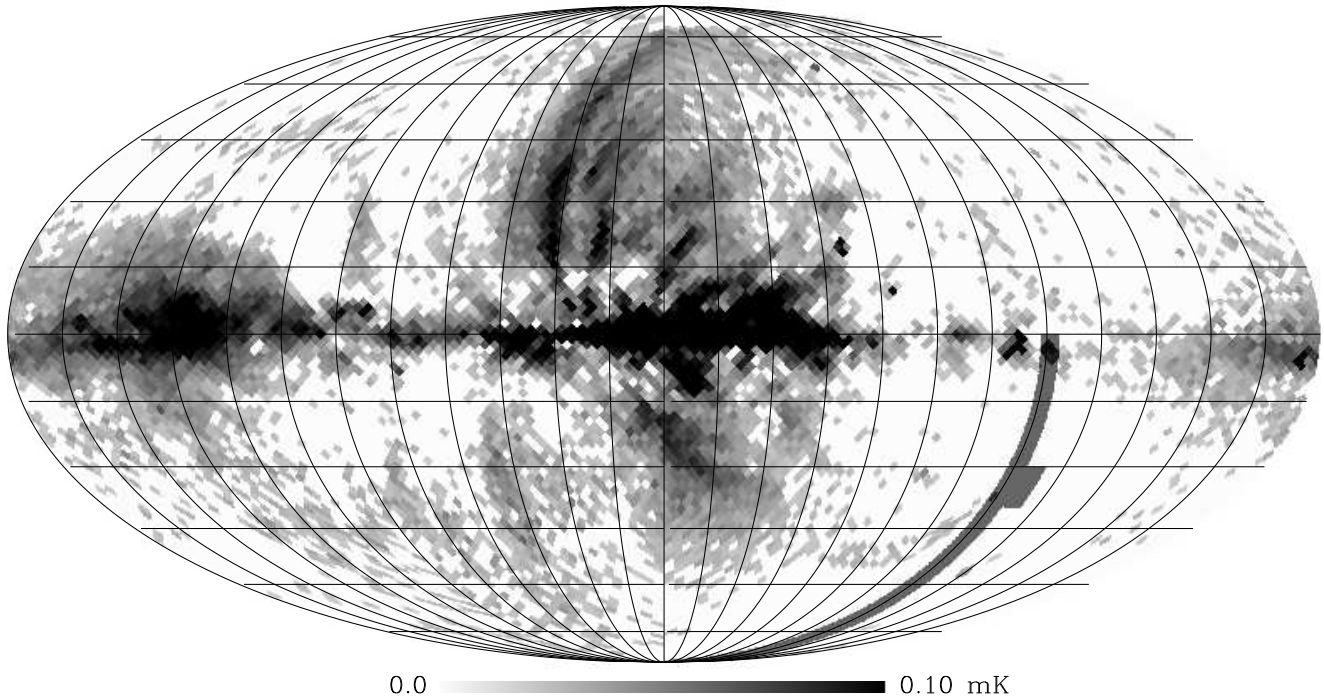


Figure 2. The PGMS strip (dark gray) plotted on the WMAP polarized emission map at 22.8 GHz (Page et al. 2007) binned in 2° pixels. Pixels with $S/N < 3$ have been blanked (white). The PGMS goes through a region clear from large emission structures preventing contamination by major local anomalies. The map is in Galactic coordinates with longitude $l = 0^\circ$ at centre and increasing leftward.

observations at higher frequencies would avoid strong Faraday Rotation effects. Carretti et al. (2005a) show that the 1.4 GHz sky is not significantly depolarized by FR only for latitudes $|b| > 50^\circ$, where the RM is about 20 rad/m^2 . That way, at 2.3 GHz the useful sky can extend to all regions with $RM < 60 \text{ rad/m}^2$ which includes all the high Galactic latitudes and the upper part of the disc (the region of interest for CMB aims) making this frequency a good trade-off.

The observations were made in four sessions from January 2006 to September 2007 with the Galileo receiver, providing right- and left-hand circular polarizations. The ATNF's Digital Filter Bank 1 (DFB1) was used to produce all four Stokes parameters, I , Q , U and V . DFB1 is equipped with an 8-bit ADC and it was configured to give 256 MHz spectrum with 128 2-MHz channels⁴. Spectra are generated by DFB1 using polyphase filters that provided high spectral channel isolation. This, in combination with the high sample precision, gives excellent protection against RFI leaking from its intrinsic frequency to other parts of the measured spectrum. This is valuable in the 13-cm band as strong RFI can be present.⁵ Recording spectra with spectral resolution

greater than required for the polarimetry analysis has allowed efficient removal of RFI-effected channels, maximising the effective useful bandwidth. Data were reduced to 30 8-MHz channels. The RFI removal typically yielded an effective total bandwidth of 160 MHz.

The source B1934-638 was used for flux calibration assuming the polynomial model by Reynolds (1994). The polarization response was calibrated using the sources 3C 138 and 0637-752, whose polarization states were determined using the Australia Telescope Compact Array (ATCA). The astronomical IAU convention for polarization angles is used: angles are measured from the local northern meridian, increasing towards the east. It is worth noting that this differs from the convention used by the WMAP data, for which the polarization angle increases westwards.

The Galactic meridian was observed in 16 $5^\circ \times 5^\circ$ fields and one $10^\circ \times 10^\circ$ enlargement. The fields are named PGMS-XX, where XX is the Galactic latitude of the field centre. Each field except PGMS-02 includes a 1° extension along b at the north edge for an actual size of $5^\circ \times 6^\circ$ and an overlap of $5^\circ \times 1^\circ$ with the next northern field.

The fields were observed with sets of orthogonal scans to give l - and b -maps (scans along Galactic longitude and latitude, respectively). Each set of maps consists of 101 (b -maps) and 121 (l -maps) scans spaced by 3 arcmin to ensure a full Nyquist sampling of the beam (FWHM = 8.9 arcmin). The same sampling interval was achieved along each scan by

⁴ DFB1 can be set up to 2048 channels. The current version DFB3 sports up to 1024 MHz BW and 8192 channels

⁵ The first observing session, in September 2005, used a Fourier-based correlator, and spectra were strongly contaminated by RFI. Subsequent use of DFB1 greatly improved the measurements.

Table 1. Main features of the PGMS observations.

Central frequency	2300 MHz
Effective bandwidth	240 MHz
Useful bandwidth ¹	160 MHz
FWHM	8.9 arcmin
channel bandwidth	8 MHz
Central Meridian	$l_0 = 254^\circ$
latitude coverage	$b = [-90^\circ, 0^\circ]$
Area size	$5^\circ \times 90^\circ$
Pixel size	$3' \times 3'$
Observation runs	Jan 2006, Sep 2006 Jan 2007, Sep 2007
Q , U beam-size pixel sensitivity (halo fields)	0.3 mK
Q , U beam-size pixel sensitivity (disc fields)	0.5 mK

¹ After RFI channel flagging.

scanning the telescope at $3^\circ/\text{min}$ and using a 1 sec sampling interval.

One full set of l - and b -maps were observed for the 6 disc fields at latitude $|b| < 30^\circ$ and the $10^\circ \times 10^\circ$ enlargement, giving final sensitivity of ~ 0.5 mK per beam-sized pixel. Over the ten high latitude fields ($|b| > 40^\circ$) where a weaker signal was expected, two full passes were made to give a sensitivity of ~ 0.3 mK per beam-sized pixel.

Prior to map-making, a linear baseline fit is removed from each scan and the ground emission contribution is estimated and cleaned up by the procedure described in Sect. 3.

The map-making procedure is based on the algorithm by Emerson & Gräve (1988), which combines l - and b -maps in Fourier space and recovers the power along the direction orthogonal to the scan, otherwise lost through the baseline removal. The algorithm is highly efficient and effectively removes residual stripes.

Tab. 1 gives a summary of the main features of the PGMS observations.

3 GROUND EMISSION

The ground emission can seriously affect continuum observations, especially in our halo fields where the emission is weak having a brightness of a few mK. Our tests have shown that the worst conditions occur in the Zenith cap at elevations above 60° where large fluctuations are observed in the data. Even though not yet fully understood, the most likely reason is the loss of ground shielding by the upper rim of the dish at large elevations. The receiver is located at the prime focus and is shielded by the dish up to this elevation, receiving only atmospheric contributions from beyond the upper rim. Above this limit the ground becomes visible, contributing a ground component that rapidly varies as the telescope scans. To avoid this contamination all PGMS observations were limited to the elevation range $\text{EL} = [30^\circ, 60^\circ]$, between the lower limit of the telescope's motion and this region of ground sensitivity.

Even though these precautions have significantly reduced the effect, some contamination is still present in the halo fields, requiring us to develop a procedure to estimate and clean the ground contribution.

3.1 Estimate and cleaning procedure

The procedure is based on making a map of the ground emission in the Azimuth–Elevation (AZ–EL) reference frame. Any AZ–EL bin gathers the contributions of data taken at different Galactic coordinates and the weak sky emission is efficiently averaged out. Since the PGMS meridian goes through low emission regions, its high latitude data are ideal for such an aim. The smooth behaviour of the ground emission enables the use of large bins, which further helps average out the sky component. Specifically, we use bin size of $\Delta\text{EL} = 1^\circ$ in EL and $\Delta\text{AZ} = 8^\circ$ in AZ⁶. The binning is performed in the instrument reference frame before the correction for the parallactic angle.

After that, at a given AZ bin, we fit a polynomial as a function of EL. This helps average residual local deviations due to, for example, strong point sources. We find most effective a sort of *quadratic running fit*: for each bin, we fit the 7 next bins to a 2-degree polynomial, and the fit result at the bin position is then used.

Data are sufficiently smoothed along AZ, and no fit is performed along that dimension. To realize a regular grid with 1.0° step also in AZ we run the procedure shifting the central AZ every 1.0° , which gives a sort of running mean.

The ground emission contamination mainly comes from the secondary lobes which are frequency dependent. We then generate maps for each frequency channel. A set of these maps is generated every run, within which we checked that the ground emission is stable and all its data can be binned together.

As example, Figure 4 reports a few AZ cuts at 2300 MHz. In a range of about 30° both in AZ and EL the ground emission contamination varies within just few dozen mK. It is worth noticing the very small AZ variations at low elevations ($\text{EL} < 45^\circ$).

Finally, the observed data are cleaned. These have a finer resolution ($3'$ instead of $60'$) and the ground emission at their actual AZ–EL position is obtained by linear interpolation through a standard Cloud-In-Cell technique.

3.2 Cleaning procedure tests

The low emission fields in the halo have been observed twice giving two independent maps taken in different runs and at different AZ and EL. That way, they are contaminated by different ground emission enabling us to test the cleaning procedure and estimate the residual contamination. The error map can be estimated as semi-difference of the two maps which cancels out the sky while leaving the noise and any residual ground emission.

An example is given by Figure 3 where the case of one of the fields with lowest emission is reported: PGMS-87. The images show Stokes Q (left) and U (right) of both the observed (top) and difference maps (bottom). No smooth is applied to better appreciate the noise features in the difference maps.

The difference maps look very good in comparison to both the sky signal and the noise level. The white noise

⁶ The ground emission is more stable in AZ allowing larger bins.

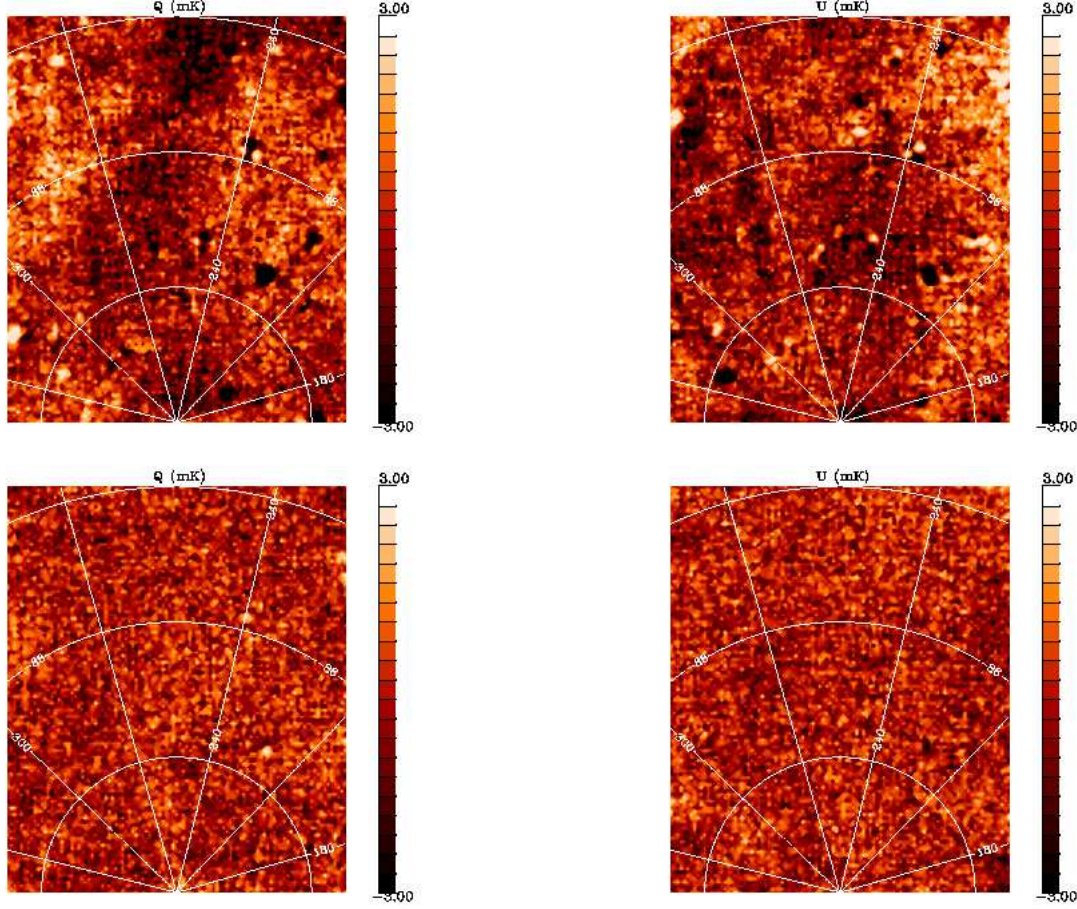


Figure 3. Q (left) and U images (right) of the observed (top) and difference maps (bottom) of the field PGMS-87 ($b=[-84^\circ, -90^\circ]$). No smooth is applied.

clearly dominates, meaning both that most of ground emission has been actually cleaned up at the level needed to measure the signal, and that the residuals do not dominate the error budget. Actually, there are *shadows* of a faint large scale behaviour, meaning that some leftover is present.

A quantitative analysis can be done measuring the angular power spectra⁷ of both the sky and the difference map. Figure 5 reports the mean of the E - and B -mode power spectra $-(E+B)/2$ – which is the most complete description of the polarized emission.

The spectrum of the sky signal is dominated by the diffuse emission at low multipole ℓ , where it follows a power law $C_\ell \propto \ell^\beta$ with a steep slope ($\beta < -2.0$). A flattening occurs at the high- ℓ end due to both noise and point sources contribution. For comparison, a white noise spectrum would be flat ($C_\ell = \text{constant}$).

The difference spectrum follows a power law as well, but it is much flatter than the sky signal. The best fit slope is $\beta_{\text{noise}} = -0.7$, which is not a pure white noise, but approaches the ideal case. Furthermore, the room between sky signal and noise enlarges at large angular scale, giving a rapidly increasing S/N, which is what does matter.

⁷ See Sect. 5 for the description of the power spectrum computation.

The ground emission has a smooth behaviour that makes the largest scales the most potentially affected. Therefore, the estimate of the residual contamination on large scales helps understand best the conditions we deal with. On 2° scale the rms fluctuation of the difference map is $N_{2^\circ} = 60 \mu\text{K}$, which is a factor 2.5 larger than that expected from white noise ($24 \mu\text{K}$) but is much smaller than the sky signal (few mK).

Actually, this is the worst case, the other fields showing even better conditions. The angular slopes range within $[-0.6, 0.0]$ and the rms noise on 2° within $[24, 55] \mu\text{K}$ and the mean values over all fields are $\bar{\beta}_{\text{noise}} = -0.4$ and $\bar{N}_{2^\circ} = 43 \mu\text{K}$. Once subtracted the pure white noise component, the effective contribution by only ground emission can be estimated in $\bar{N}_{\text{grnd}, 2^\circ} = 36 \mu\text{K}$. With such results the ground emission can be assumed under control with negligible effects on our final maps.

4 PGMS MAPS

Maps of the Stokes parameters Q , U and the polarized intensity L of the PGMS meridian are shown in Fig. 6, 7, and 8, while Fig. 9 displays the whole $10^\circ \times 10^\circ$ enlargement (field PGMS-34). All images are smoothed with a

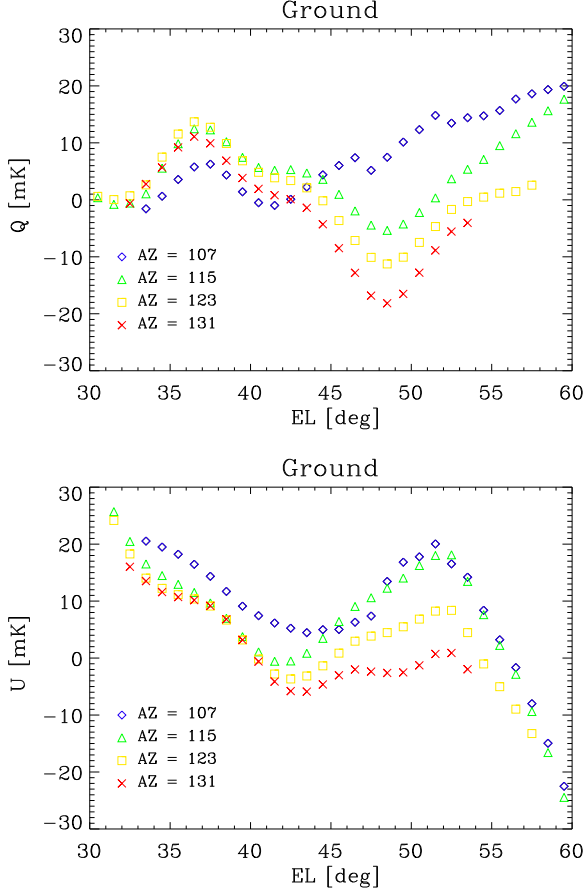


Figure 4. Examples of azimuth cuts of the ground emission maps of both Q (top) and U (bottom): the case of the 2300 MHz channel of the September 2007 run is reported.

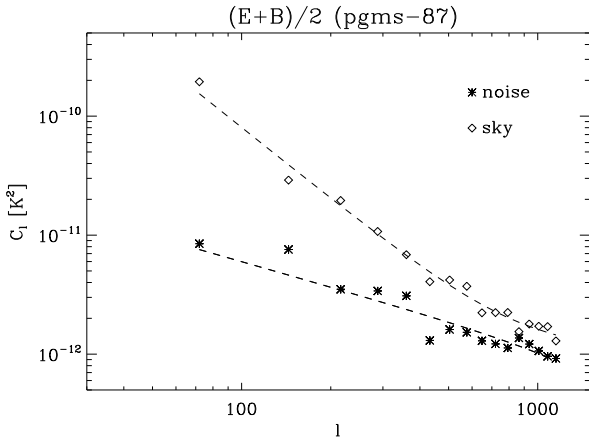


Figure 5. Power spectrum of the mean $(E+B)/2$ of E - and B -Modes measured for the PGMS-87 polarized emission: sky emission (diamonds) and difference map (stars). The best fit curves are also reported (dashed).

Table 2. Polarization flux limits S_p^{lim} used to select the polarized sources. Different limits have been used depending on the Galactic latitude range (b -range).

b -range	S_p^{lim} [mJy]
$[-10^\circ, 0^\circ]$	40
$[-20^\circ, -10^\circ]$	30
$[-30^\circ, -20^\circ]$	20
$[-40^\circ, -30^\circ]$	15
$[-90^\circ, -40^\circ]$	10

Gaussian filter of $\text{FWHM} = 6'$ to give a better idea of the sensitivity on beam-size scale, for an effective resolution of $\text{FWHM} = 10.7'$. All data at latitude $|b| > 30^\circ$ are plotted with the same intensity range to show clearly the power and morphological differences. The disc fields ($|b| < 30^\circ$) require a more extended scale. The two strongest sources present in our data (Pic A and NGC 612 in field PGMS-34 and PGMS-77, respectively) have been blanked before the map generation of their fields. Without blanking the high brightness range does not allow the map-making procedure to work properly, generating artefacts in the maps.

The disc has the strongest emission. Visually, this extends up to latitude $|b| \sim 20^\circ$ with little variation of emission power. At higher latitudes, the emission starts to decrease up to the halo where it settles on levels one order of magnitude lower.

The fact that the disc emission is clearly visible and brighter than the halo is new result, not apparent from previous observations carried out at lower frequencies where the disc is strongly depolarized up to $|b| \sim 30^\circ$. This enables the analysis of disc properties, not accessible to previous surveys, to pinpoint the location of the disc-halo transition in polarization, a question unsolved so far because of either strong depolarization (at 1.4 GHz) or insufficient sensitivity (at 23 GHz). A more quantitative analysis is given in Sect. 5, but the visual inspection of the maps clearly shows that it starts at $|b| \sim 20^\circ$.

The emission of the halo has a smooth behaviour with the power mostly residing on large angular scales. The disc emission is smooth too, at least at latitudes higher than $|b| = 6^\circ - 7^\circ$. Only close to the Galactic plane the pattern has a more patchy appearance. This supports the view that FR depolarization effects are marginally significant in the disc, and are relevant only in a narrow belt a few degrees wide across the Galactic plane.

Several polarized point sources are visible, especially in the halo where the diffuse emission fluctuations are smaller. To enable a cleaner analysis of the diffuse component the sources are identified, fitted and subtracted from the maps. Each source is located by a 2D-Gaussian fit of the stronger component, either Q or U . Its position is then constrained in the fit of the second and weaker component to improve the fit robustness. A polarization flux limit selection is applied with threshold set to ensure S/N ratios of at least 5–10. The amplitude of fluctuations in the maps is dominated by sky emission (rather than by the instrument sensitivity), which varies along the PGMS meridian. The threshold we use is therefore function of the Galactic latitude, running from 10 mJy at high latitudes up to 40 mJy near the Galactic plane (Tab. 2).

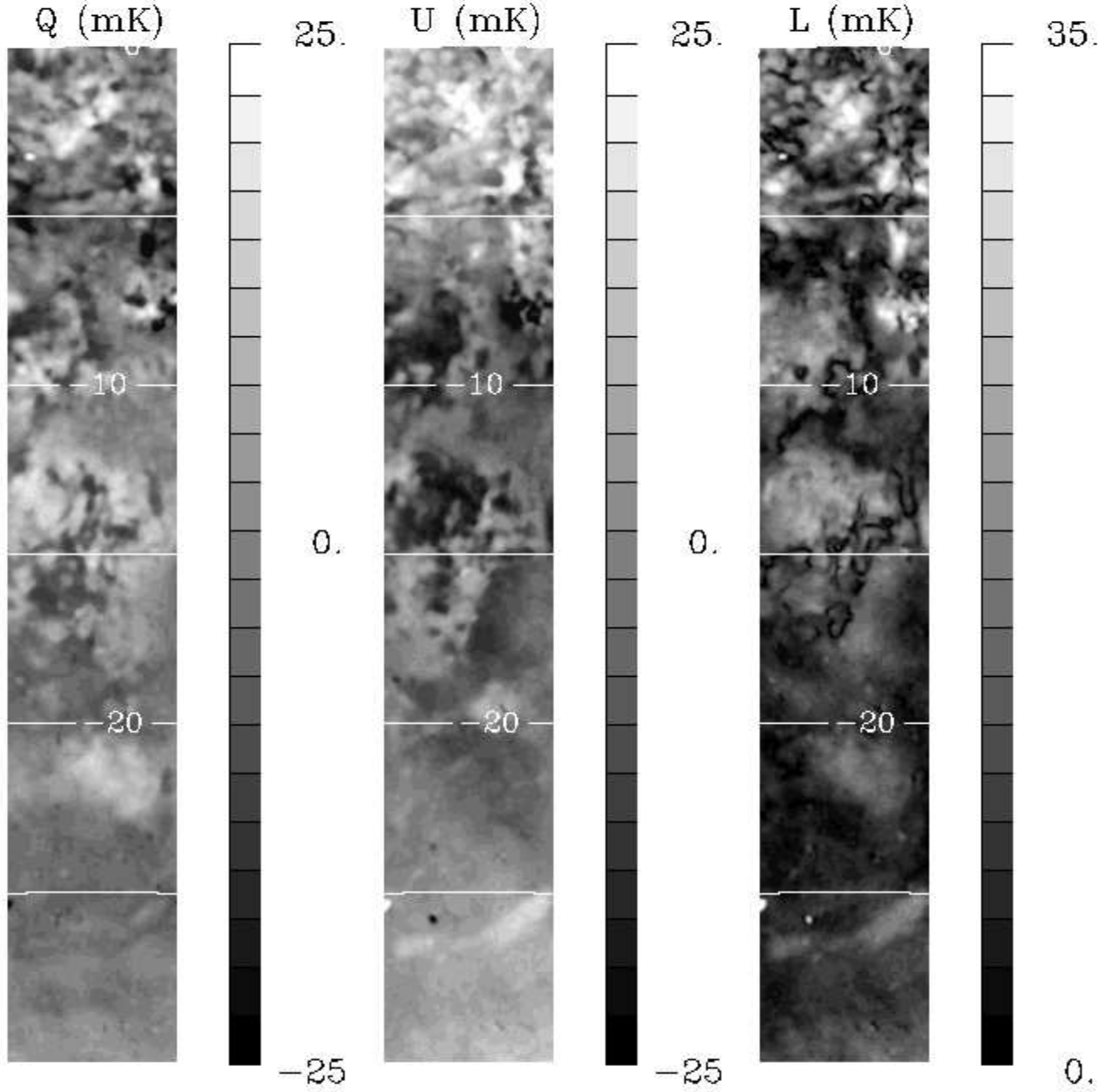


Figure 6. Q (left), U (mid), and polarized intensity $L = \sqrt{Q^2 + U^2}$ images (right) of the six PGMS fields in the latitude range $b = [-30^\circ, 0^\circ]$ (PGMS-27 throughout PGMS-02).

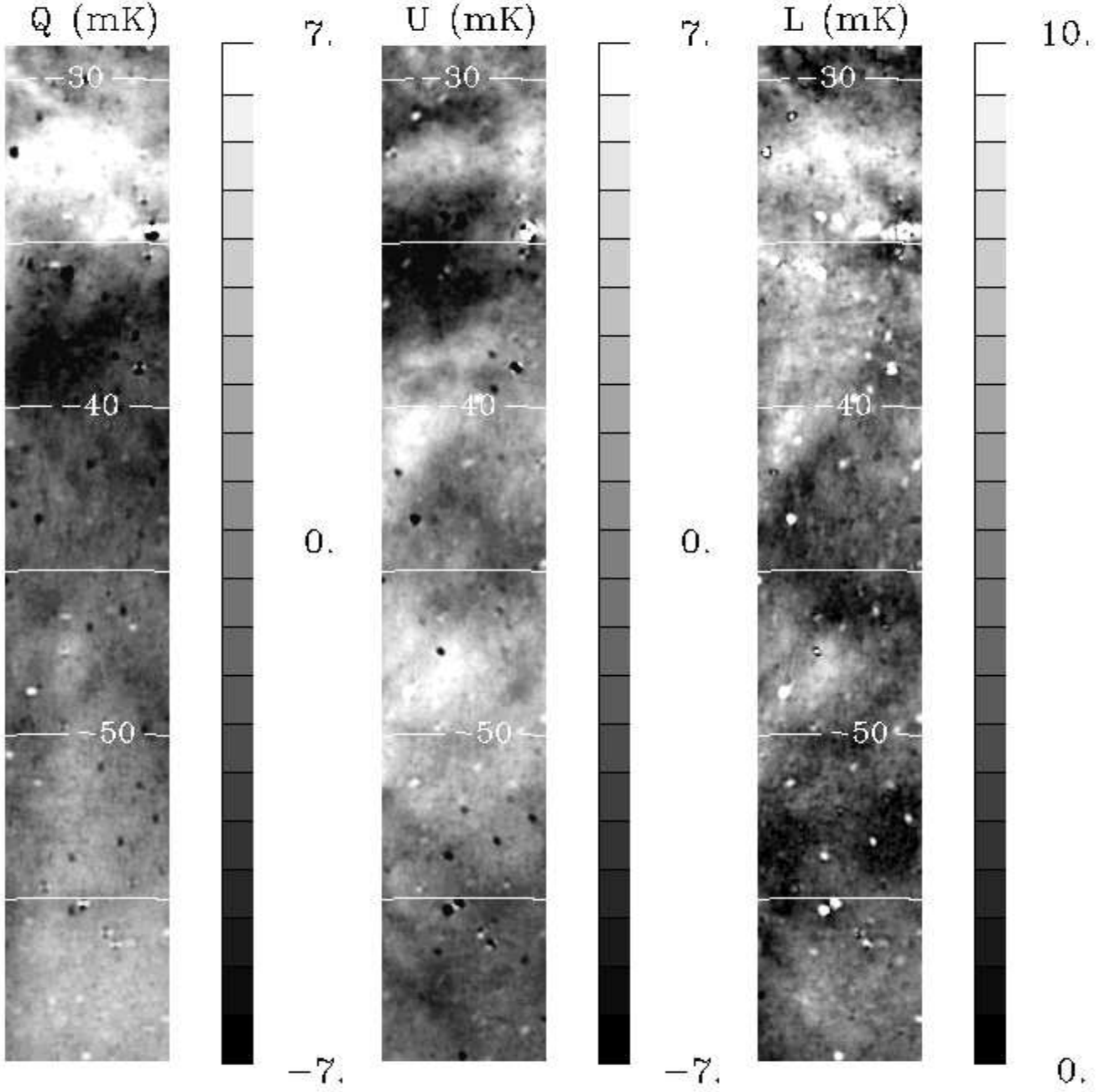


Figure 7. As for Fig. 6 but in the range $b = [-60^\circ, -30^\circ]$ (PGMS-57 throughout PGMS-34: of the latter only the 5° across the meridian $l = 254^\circ$ are imaged).

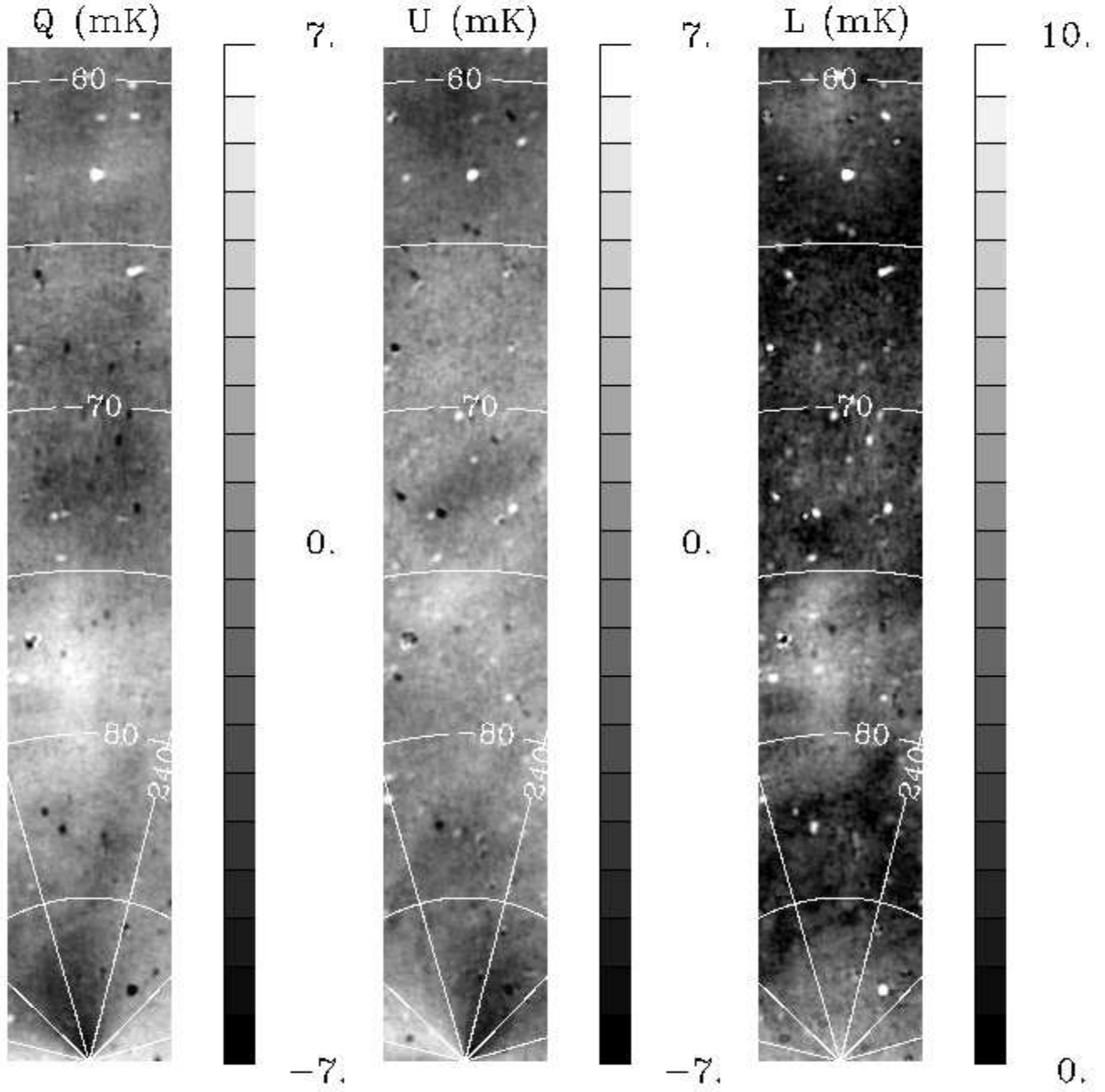


Figure 8. As for Fig. 6 but in the range $b = [-90^\circ, -60^\circ]$ (PGMS-87 throughout PGMS-62).

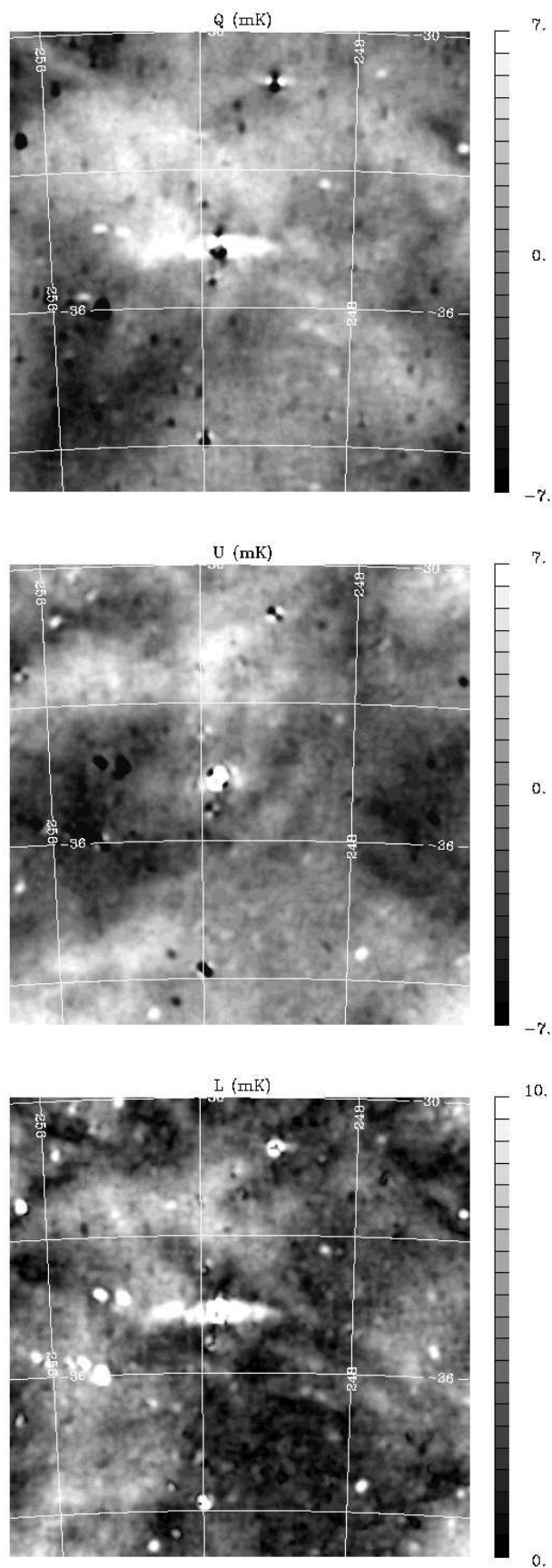


Figure 9. Q (top), U (mid), and L images (bottom) of the whole $10^\circ \times 10^\circ$ enlargement (fields PGMS-34).

In this work, the point source identification is carried out only for cleaning purposes. The catalogue and a detailed analysis of their properties are subject of a forthcoming paper (Bernardi et al. 2009, in preparation).

5 ANGULAR POWER SPECTRA

The angular power spectra (APS) of E - and B -Mode of the polarized emission have been computed for each field. They account for the 2-spin tensor nature of the polarization and give a full description of the polarized signal and its behaviour across the range of angular scales. In addition, the E - and B -Modes are the quantities predicted by the cosmological models enabling a direct comparison with the CMB.

To cope with both the non-square geometry and the blanked pixels in the location of the two brightest sources, we use a method based on the two-point correlation functions of the Stokes parameters Q and U described by Sbarra et al. (2003). The correlation functions are estimated on the Q and U maps of the regions as

$$\tilde{C}^X(\theta) = X_i X_j \quad X = Q, U \quad (1)$$

where X_i is the emission in pixel i map X , and i and j identify pixel pairs at distance θ . Data are binned with pixel-size resolution. Power spectra $C_\ell^{E,B}$ are obtained by integration

$$C_\ell^E = W_\ell^P \int_0^\pi [\tilde{C}^Q(\theta) F_{1,\ell 2}(\theta) + \tilde{C}^U(\theta) F_{2,\ell 2}(\theta)] \sin(\theta) d\theta \quad (2)$$

$$C_\ell^B = W_\ell^P \int_0^\pi [\tilde{C}^U(\theta) F_{1,\ell 2}(\theta) + \tilde{C}^Q(\theta) F_{2,\ell 2}(\theta)] \sin(\theta) d\theta \quad (3)$$

where $F_{1,\ell m}$ and $F_{2,\ell m}$ are functions of Legendre polynomials (see Zaldarriaga 1998 for their definition), and W_ℓ^P is the pixel window function accounting for pixel smearing effects.

We tested the procedure using mock maps generated from a known input power spectrum by the procedure *synfast* of the software package HEALPix (Górski et al. 2005). The input spectra are power laws with different slopes; for each slope we generated 100 mock maps and compute their APS. The mean of the 100 APS reproduced correctly the input spectrum and its slope, with the exception of an excess at the largest scales, mainly at the first two multipole bands. To account for this we corrected our spectra for the fractional excess estimated from the simulation as the ratio between the mean of the computed and input spectra.

For a cleaner measure of the diffuse component, the point sources are subtracted from the polarization maps. The S/N limit used to identify the sources is set to avoid picking up diffuse emission fluctuations and altering the apparent synchrotron emission properties.

The E - and B -mode spectra C_ℓ^E and C_ℓ^B have been computed for the 17 fields along with their mean $C_\ell^{EB} = (C_\ell^E + C_\ell^B)/2$. Artificial fluctuations are generated on E and B spectra because of the limited sky coverage of the individual areas, but their mean suffers less from that effect and is a more accurate estimator in case of equal distribution of power between the two modes, like for the Galactic emission. In addition, C_ℓ^{EB} gives a full description of the polarized emission which the two individual spectra cannot give separately. Therefore we mostly use the mean spectrum

$(E+B)/2$ to investigate emission behaviour and properties in the following analysis.

Figure 10 shows C_ℓ^{EB} for all the fields. As an example of all the three spectra, Fig. 11 shows those of the two fields PGMS-52, which is from the low emission halo, and PGMS-34, our biggest field and the area observed by the BOOMERanG experiment. All spectra are reported as computed without correction for the window functions. In most fields the spectra follow a power law behaviour that flattens at the high multipole end because of the noise contribution. The exceptions are in four fields closest to the Galactic plane (PGMS-17 to PGMS-02) where a power law modulated by the beam window function dominates everywhere. The point source cleaning is quite effective, with no evidence of their contribution in the spectra.

We fit the angular power spectra to a power law modulated by the beam window function W_ℓ^B and a constant term N , which account for synchrotron component and noise, respectively:

$$C_\ell^X = \left[C_{200}^X \left(\frac{\ell}{200} \right)^{\beta^X} W_\ell^B + N \right] W_\ell^P, \quad (4)$$

where $X = E, B, EB$ denotes E -Mode, B -Mode, and their mean $(E+B)/2$. Possible residual contributions by point sources are accounted for by the constant term.

Plots of the best fits are shown in Fig. 10 and 11, while the parameters of the synchrotron component are reported in Tab. 3.

To analyse the behaviour of the synchrotron component, the best fit spectra are plotted together in Fig. 12 where they are also extrapolated to 70 GHz for comparison with the CMB signal. A frequency spectral index $\alpha = -3.1$ is used for the extrapolation (Bernardi et al. 2004).

Distinguishing fields in terms of their spectral slopes, Fig. 12 and Fig. 13 shows the presence of two well defined regions:

- The high and mid latitude fields ($b = [-90^\circ, -20^\circ]$), with steep spectra ($\beta < -2.0$); slopes are distributed over the wide range $\beta \sim [-3.0, -2.0]$ (except few outliers). There is no clear trend with latitude and the slopes are rather uniformly distributed. The median⁸ is $\beta_{\text{med}}^{EB} = -2.6$ (Tab. 5). The dispersion $\sigma_{\beta^{EB}} = 0.24$ is significantly larger than the individual measurement errors, meaning that this wide spread is an intrinsic property of the synchrotron emission at these latitudes.
- The low latitude fields ($b = [-20^\circ, 0^\circ]$), which show inverted spectra ($\beta > -2.0$). The slopes lie in a much narrower range ($\beta^{EB} = [-1.90, -1.75]$) with dispersion $\sigma_{\beta^{EB}} = 0.08$ (Tab. 5). All spectra have mean slope $\bar{\beta}^X = -1.8$, which can be considered the typical value of this region.

This change from steep to inverted spectra is quite sudden and clearly separates two different environments: the mid-high latitudes, characterised by a smooth emission with most of the power on large angular scales, and the disc fields, whose power is more evenly distributed with a slight predominance of the small scales.

⁸ We prefer to use the median to estimate the typical angular slope in this region because of the possible significant deviations by the outliers.

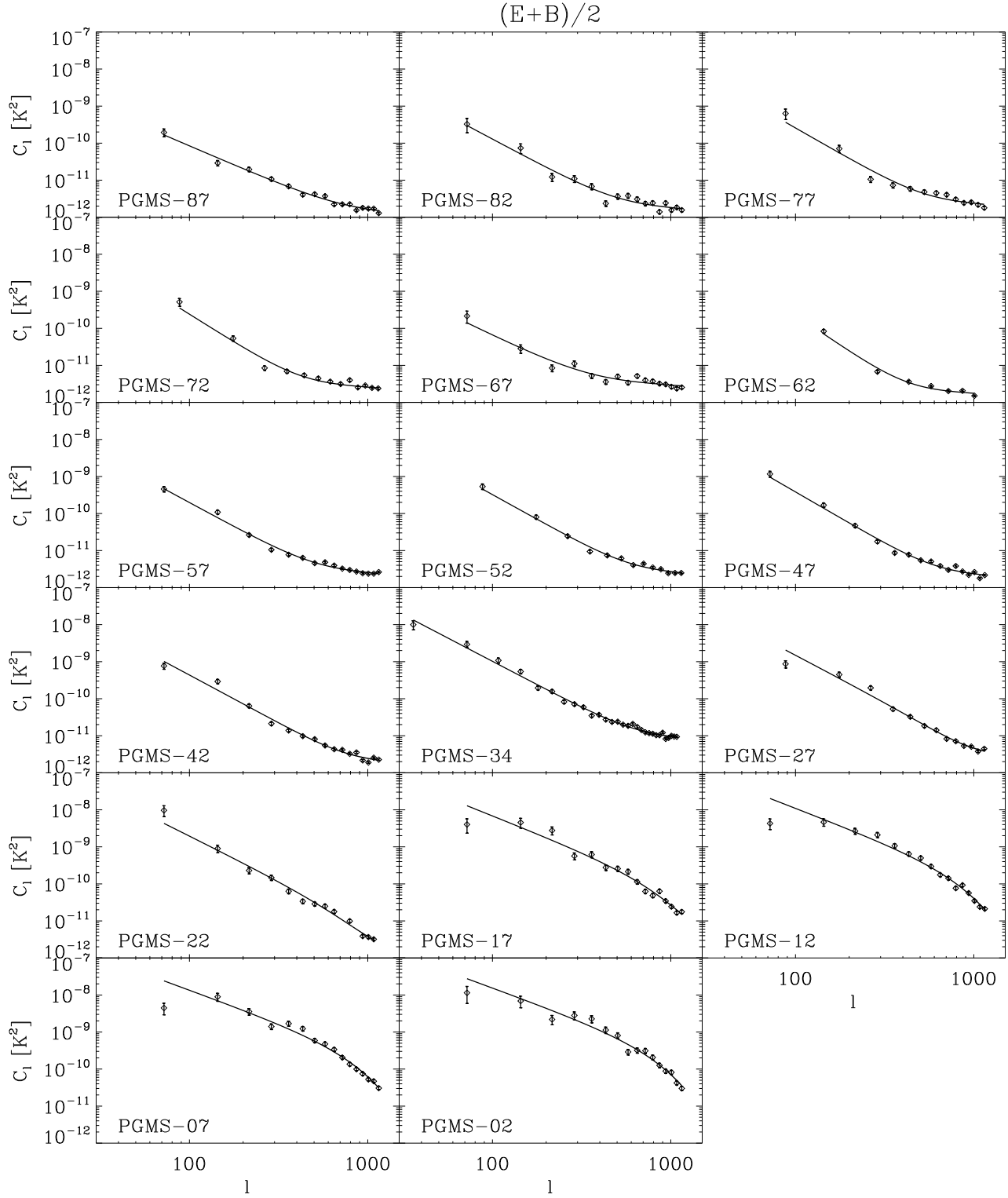


Figure 10. Angular power spectra C_ℓ^{EB} of the 17 PGMS fields. Both the measured spectra (diamonds) and the best fit curve (solid) are plotted.

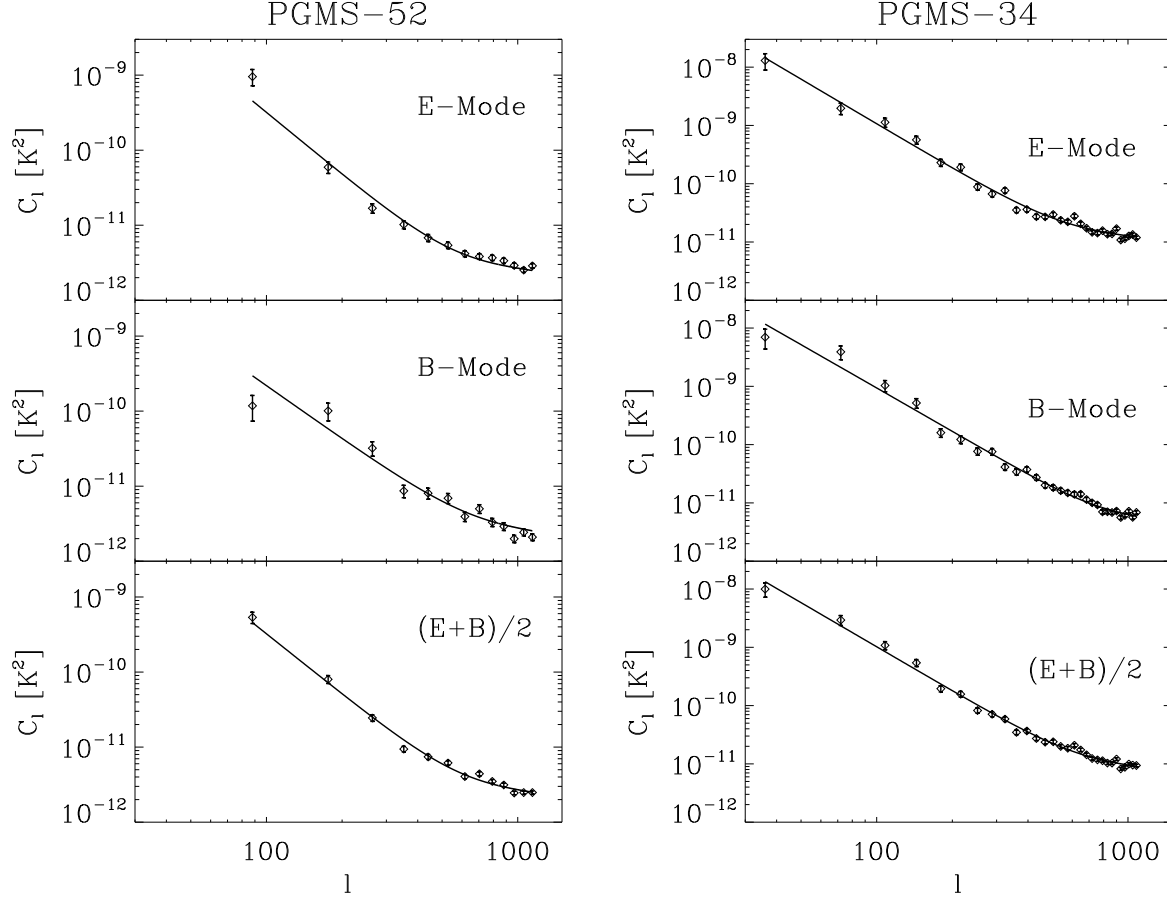


Figure 11. Angular power spectrum of E -Mode (top), B -Mode (mid), and their mean $(E+B)/2$ of the two fields PGMS-52 (left) and PGMS-34 (right). Both the measured spectra (diamonds) and the best fit curve (solid) are plotted.

Table 3. Best fit amplitude C_ℓ^X and angular spectral slope β^X of the PGMS fields ($X = E, B, EB$ denotes E -, B -Mode, and $(E+B)/2$, respectively).

Field	$C_{200}^E [\mu K^2]$	β^E	$C_{200}^B [\mu K^2]$	β^B	$C_{200}^{EB} [\mu K^2]$	β^{EB}
PGMS-87	26.9 ± 1.6	-2.21 ± 0.07	11.3 ± 0.7	-1.74 ± 0.07	19.9 ± 1.4	-2.08 ± 0.09
PGMS-82	16.2 ± 3.3	-2.36 ± 0.35	18.0 ± 3.0	-2.51 ± 0.27	21.7 ± 2.8	-2.57 ± 0.21
PGMS-77	41.6 ± 6.4	-3.05 ± 0.27	33.8 ± 3.6	-2.47 ± 0.16	38.4 ± 4.5	-2.75 ± 0.19
PGMS-72	40.1 ± 4.1	-3.08 ± 0.16	14.9 ± 2.8	-2.81 ± 0.33	29.7 ± 2.7	-3.03 ± 0.15
PGMS-67	15.6 ± 2.0	-2.17 ± 0.19	5.4 ± 1.1	-2.23 ± 0.34	12.6 ± 1.6	-2.35 ± 0.20
PGMS-62	28.9 ± 3.1	-3.27 ± 0.22	19.1 ± 3.4	-3.35 ± 0.40	24.1 ± 1.9	-3.27 ± 0.17
PGMS-57	46.7 ± 3.4	-2.62 ± 0.10	16.6 ± 2.2	-2.54 ± 0.21	32.4 ± 1.7	-2.61 ± 0.07
PGMS-52	47.9 ± 4.4	-2.74 ± 0.13	42.7 ± 5.9	-2.36 ± 0.17	51.3 ± 3.2	-2.66 ± 0.08
PGMS-47	59.8 ± 7.7	-2.91 ± 0.20	49.7 ± 4.3	-2.56 ± 0.13	56.3 ± 3.1	-2.78 ± 0.08
PGMS-42	79 ± 11	-2.76 ± 0.19	61.9 ± 6.3	-2.24 ± 0.14	74.1 ± 4.0	-2.57 ± 0.08
PGMS-34	183.5 ± 8.5	-2.54 ± 0.07	171.8 ± 9.0	-2.46 ± 0.07	180.0 ± 7.1	-2.51 ± 0.06
PGMS-27	287 ± 58	-2.41 ± 0.24	131 ± 19	-2.17 ± 0.19	263 ± 20	-2.51 ± 0.09
PGMS-22	550 ± 100	-2.54 ± 0.17	246 ± 39	-2.60 ± 0.16	376 ± 31	-2.39 ± 0.08
PGMS-17	2090 ± 260	-2.00 ± 0.10	1270 ± 140	-1.67 ± 0.08	1840 ± 190	-1.91 ± 0.08
PGMS-12	2800 ± 200	-1.86 ± 0.05	3160 ± 410	-1.82 ± 0.09	3070 ± 240	-1.85 ± 0.06
PGMS-07	3850 ± 380	-1.77 ± 0.07	4120 ± 340	-1.75 ± 0.06	4030 ± 340	-1.76 ± 0.06
PGMS-02	4500 ± 280	-1.69 ± 0.04	4860 ± 880	-1.90 ± 0.13	4610 ± 540	-1.76 ± 0.09

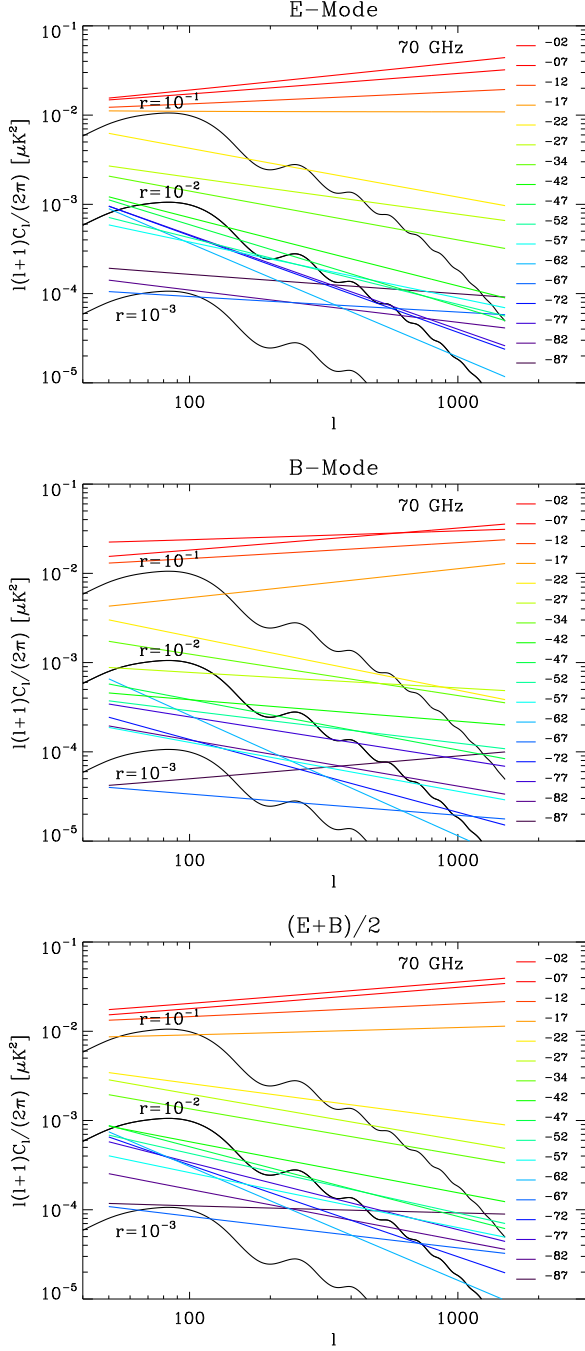


Figure 12. Best fits to the spectra of E -Mode (top), B -Mode (mid), and their mean $(E+B)/2$ (bottom) of all PGMS fields. The plot reports only the power law component which describes the synchrotron emission. All PGMS fields are plotted together for a direct comparison of the behaviour with the Galactic latitude. The colour code goes from blue throughout red by a rainbow palette for the areas from the south Galactic pole (PGMS-87) throughout the Galactic plane (PGMS-02), respectively. The spectra are scaled to 70 GHz for a comparison with the CMB signal (frequency spectral index $\alpha = -3.1$). CMB B -Mode spectra for different values of tensor-to-scalar power ratio r are shown for comparison. The quantity plotted here is $\ell(\ell+1)/(2\pi) * C_\ell^X$, which provides a direct estimate of the power distribution through the angular scales: a flat spectrum means the power is evenly distributed; a decreasing spectrum (steep) is led by the largest scales; a rising spectrum (inverted) is led by the smallest scales.

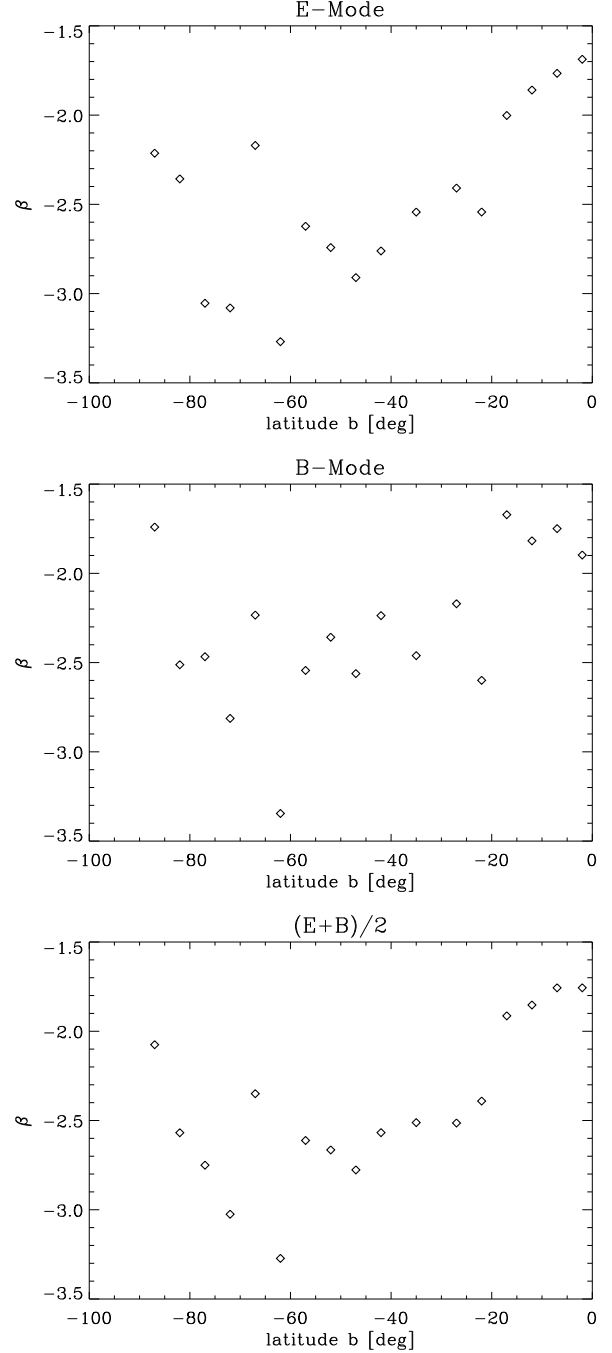


Figure 13. Angular spectral slopes of the PGMS fields plotted versus the field's centre latitude for E -Mode (top), B -Mode (mid), and $(E+B)/2$.

Does this change indicate an intrinsic feature of the polarized emission of the disc, or is it the effect of Faraday modulation that transfers power from large to small angular scales in the low latitude fields? The answer is unclear with the information available, but some points can be noted. In the disc the ISM is more turbulent than in the halo and the intrinsic emission might have more power on small angular scales. In addition, the line of sight goes through much more ISM including more distant structures, which is expected to give more power to the small angular

Table 4. Mean ($\bar{\beta}^X$), median (β_{med}^X), and dispersion (σ_{β}^X) of the angular slopes at mid-high Galactic latitudes for all the three spectra $X = E, B, EB$.

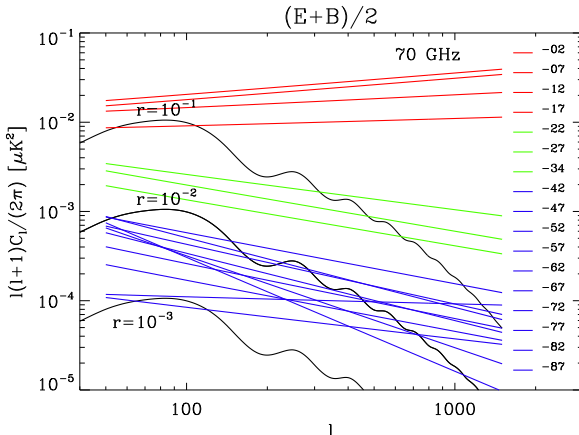
MID-HIGH latitudes			
X	$\bar{\beta}^X$	β_{med}^X	σ_{β}^X
E	-2.67	-2.62	0.34
B	-2.39	-2.46	0.27
EB	-2.57	-2.57	0.24

Table 5. As for Tab. 5 but for low Galactic latitudes.

LOW latitudes			
X	$\bar{\beta}^X$	β_{med}^X	σ_{β}^X
E	-1.83	-1.81	0.14
B	-1.78	-1.78	0.10
EB	-1.82	-1.80	0.08

scales. Also the smooth emission of the two highest latitude disc fields (PGMS-12 and PGMS-17) make the presence of significant FR depolarisation unlikely. Finally, we have computed the power spectrum of the individual frequency channels to search for a possible variation of the angular slope with frequency. Since the lowest frequencies would be more affected, steeper spectra at highest frequencies would support the presence of FR effects. We find that all the four disc fields have non-significant slope variation compatible with zero within 1.0–1.5 sigma, with the only exception of PGMS-02 which approaches 2-sigma. All these considerations support the intrinsic nature of the change of emission properties, with maybe the exception of PGMS-02. However, more data and analyses are required to confirm this result.

Distinguishing fields according to the amplitude of their emission, three distinct regions are evident (Fig. 14) since the mid-high latitude area identified by spectral slope splits

**Figure 14.** As for bottom panel of Fig. 12 except that all spectra of the fields of the same amplitude region are plotted with same colour: blue ($b = [-90^\circ, -40^\circ]$), green ($b = [-40^\circ, -20^\circ]$), and red ($b = [-20^\circ, 0^\circ]$).

into an halo ($b = [-90^\circ, -40^\circ]$) and transition region ($b = [-40^\circ, -20^\circ]$). The three areas are:

- Halo ($b = [-90^\circ, -40^\circ]$): the emission is weak here and, scaled to 70 GHz, is between the peaks of CMB models with $r = 10^{-3}$ and $r = 10^{-2}$. The weakest fields (PGMS-87 and PGMS-67) match models with $r = 10^{-3}$. The fluctuations from field to field dominate with no clear trend with latitude. A weak trend might be present with the emission power increasing toward lower latitudes, but the effect is a minor in comparison to the dominant field-to-field fluctuations.

- Galactic disc ($b = [-20^\circ, 0^\circ]$): the emission is stronger, about two orders of magnitude brighter than that of the halo. Within the area there is no large variation of the emission power, but slight increase toward the Galactic plane is evident.

- Transition strip ($b = [-40^\circ, -20^\circ]$): here a transition between the faint high latitudes and the bright disc occurs. This is clearer at large scales, where the northernmost field (PGMS-22) is almost as bright as the weakest disc field (PGMS-17) and the southernmost field approaches the upper end of the halo brightness range.

Therefore, considering both amplitude and slope, we can distinguish three latitude sections: two main regions (disc and high latitudes) well distinguished by both emission power and structure of the emission, and an extended transition about 20° wide connecting them.

A first important consequence is the identification of a clear transition between disc and halo. The sudden change in the angular spectral slope at $|b| \sim 20^\circ$ and the approximately constant emission power from the Galactic plane up to that transition clearly separate the 20° equatorial zone from the higher latitudes. Characterised by a more complex structure of the ISM this area can be associated with the Galactic disc.

A second environment characterised by steep spectra and low emission is clearly present above $|b| = 40^\circ$. Both angular slope and amplitude exhibit wide fluctuations without any clear trend with latitude. This high Galactic latitude section is thus just one environment in terms of polarized synchrotron emission properties. Characterised by a smoother emission and simpler ISM structure, this area can be associated to the Galactic halo.

The emission of the halo section is very weak. In spite of large fluctuations, once scaled to 70 GHz the synchrotron component is equivalent to r values between 1×10^{-3} and 7×10^{-3} , which matches the weakest areas observed so far in polarization. It is worth noticing that the best PGMS fields (PGMS-87 and PGMS-67) are the areas with weakest polarized synchrotron emission observed so far.

The high Galactic latitudes above 40° are thus just one environment, at least in a low emission region not contaminated by local anomalies like the area intersected by PGMS. This is very important for CMB investigations, since it tells that, in principle, it is possible to find large areas with optimal conditions (extended over 50° , in the PGMS case).

It is thus important to measure the emission properties of the PGMS halo section as a whole. To do so we average the spectra of all 10 halo fields. The mean spectrum and its best fit are plotted in Fig. 15; Tab. 6 gives the best fit parameters; the extrapolation to 70 GHz is shown in Fig. 16. The angular slope is $\beta^X \sim -2.6$ for all the three spectra

Table 6. Best fit amplitude C_ℓ^X and angular spectral slope β^X of the mean spectrum of the PGMS halo section ($X = E, B, EB$ denotes E -, B -Mode, and $(E+B)/2$, respectively).

Field	$C_{200}^E [\mu\text{K}^2]$	β^E	$C_{200}^B [\mu\text{K}^2]$	β^B	$C_{200}^{EB} [\mu\text{K}^2]$	β^{EB}
PGMS HALO	40.7 ± 3.2	-2.65 ± 0.10	28.5 ± 3.0	-2.64 ± 0.12	35.5 ± 2.9	-2.60 ± 0.09

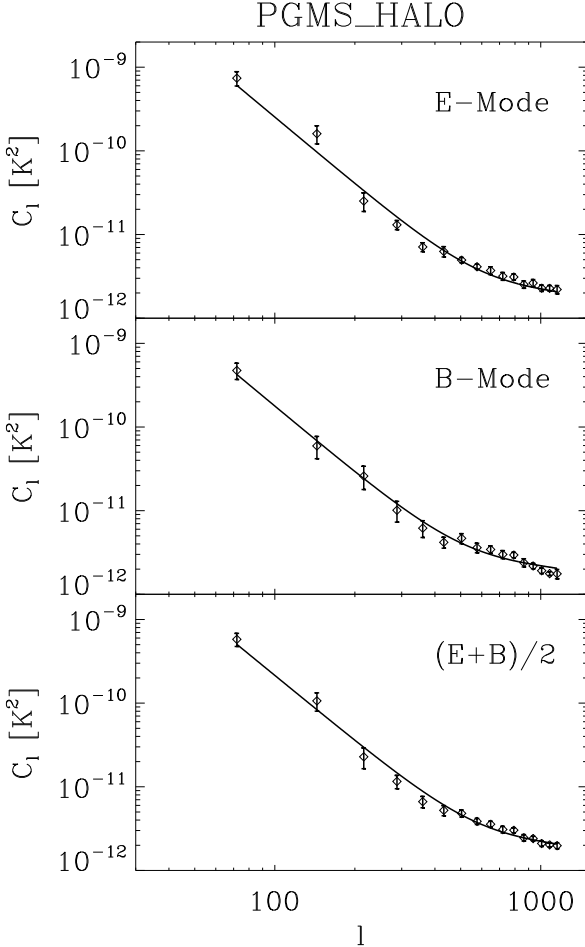


Figure 15. Mean of the power spectra of the halo fields ($b = [-40^\circ, -90^\circ]$) for E -Mode (top), B -Mode (mid), and their mean $(E+B)/2$ (bottom). Both the mean of the measured spectra (diamonds) and its best fit curve (solid) are plotted.

E , B , and $(E+B)/2$ and is thus be considered the typical slope of the halo section. It is worth noticing that this value matches the slope measured at high latitudes by WMAP at 22.8 GHz (Page et al. 2007). This means that the power distribution through the angular scales is the same at 2.3 and 22.8 GHz implying that FR effects are negligible already at 2.3 GHz. If present, the FR effects would have transferred power from large to small scales modifying the spectral shape.

Once scaled to 70 GHz, the amplitude is equivalent to

$$r_{\text{halo}} = (3.3 \pm 0.4) \times 10^{-3}, \quad (5)$$

roughly in the middle of the range covered by the individual

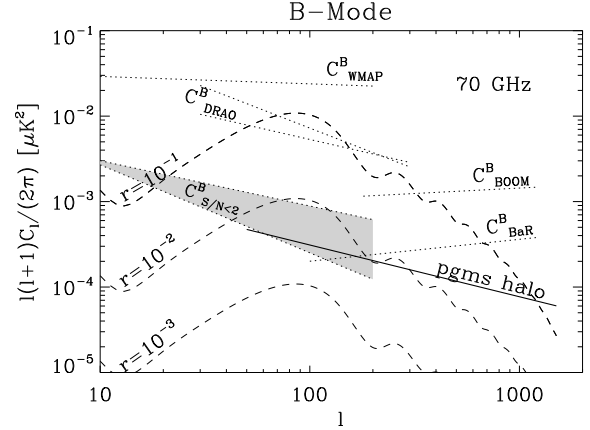


Figure 16. Best fit of the mean halo spectrum C_ℓ^{EB} scaled to 70 GHz (solid) alongside CMB B -Mode spectra for different r values (dashed). The mean synchrotron contamination at all high Galactic latitudes is also shown for comparison (C_{WMAP}^B) together with the previous estimates in other low emission regions: $C_{S/N<2}^B$ (shaded area), C_{DRAO}^B , C_{BOOM}^B , and C_{BaR}^B (see Fig. 12 for details).

fields. As mentioned earlier, this is a very low level and corresponds to the faintest areas observed previously, which thus seem to be more the normal condition of the low emission regions rather than *lucky* exceptions.

Finally, the field PGMS-34 deserves special mention as the area observed by the experiment BOOMERanG. It lies in the transition region, and although at the high-latitude end of this zone, has emission about five times greater than fields in the halo. It is suitable for measuring the stronger E -mode (the aim of the 2003 BOOMERanG flight), but our results identify more suitable fields for detecting the B -mode.

6 DUST EMISSION IN THE PGMS HALO SECTION

The dust emission is the other most significant foreground for CMB observations. It has a positive frequency spectral index and dominates the foreground budget at high frequency.

An estimate of the local dust contribution in the same portion of halo covered by the PGMS is thus important to understand the overall limits of a CMB B -Mode detection in that area.

However, no polarized dust emission has been detected over the PGMS region, and even the total intensity dust map of WMAP is noise dominated in that area.

We then use the Finkbeiner, Davis & Schlegel (1999) model of the total intensity dust emission applying an assumed polarization fraction. First, we generate maps at

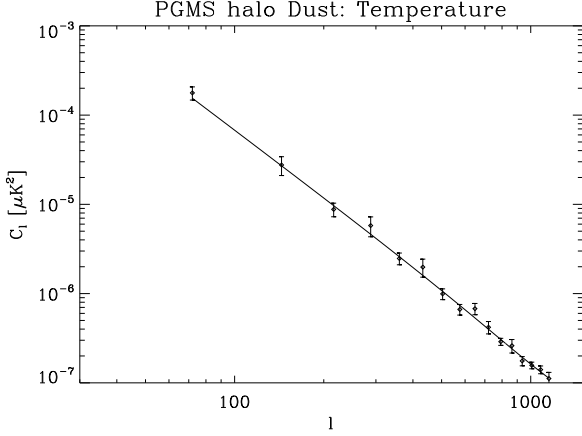


Figure 17. Temperature power spectrum of the dust emission model at 94 GHz in the halo section of the PGMS ($b = [-90^\circ, -40^\circ]$). The spectrum is the mean of those measured in the individual PGMS fields. Both the mean of the measured spectra (diamonds) and its best fit curve (solid) are plotted.

Table 7. Best fit amplitude C_{200}^T and angular spectral slope β_d^T of the mean Temperature dust spectrum at 94 GHz in the halo section of the PGMS ($|b| > 40^\circ$).

Field	C_{200}^T [μK^2]	β_d^T
PGMS halo Dust	$(12.0 \pm 1.4) \times 10^{-6}$	-2.50 ± 0.14

94 GHz using their model-8 for each of the 10 PGMS fields at $|b| > 40^\circ$. The temperature power spectra of each are then computed and averaged together to estimate the mean conditions of the whole $5^\circ \times 50^\circ$ section. Figure 17 shows both the mean spectrum and its best fit, whose parameters are reported in Tab. 7. Within the errors, the angular slope matches well that of the synchrotron.

The total polarized spectrum is estimated from this temperature spectrum assuming a polarization fraction $f_{\text{pol}} = 0.10$, as inferred for high Galactic latitudes from the Archeops experiment data (Benoit et al. 2004). The spectrum is further divided by two to account for an even distribution of power between E - and B -Mode, a reasonable assumption for the Galactic emission.

For frequency extrapolations, we use a single Planck function modulated by a power law $T_d \propto \nu^{\alpha_d} / (e^{\frac{h\nu}{kT}} - 1)$ with index $\alpha_d = 2.67$ and temperature $T = 16.2$ K, which well reproduces the Finkbeiner et al. (1999) model in the range $[70, 150]$ GHz. It is worth noticing that at 94 GHz that function is well approximated by a simpler power law with index $\alpha_d^{\text{PL}} = 1.5$, consistent with the 5-yr WMAP result of $\alpha_d^{\text{WMAP}} = 1.8 \pm 0.3 \pm 0.2$ (statistical and systematic error, Gold et al. 2009).

Our estimate of the B -Mode polarized dust spectrum at 70 GHz is given in Fig. 18. At this frequency the two components of Galactic polarized emission are approximately equal over the halo portion of PGMS, and so the total polarized foreground is at a minimum. This frequency is mildly dependent on assumed polarized fraction of the synchrotron component: alternate assumptions of five percent or twenty per-

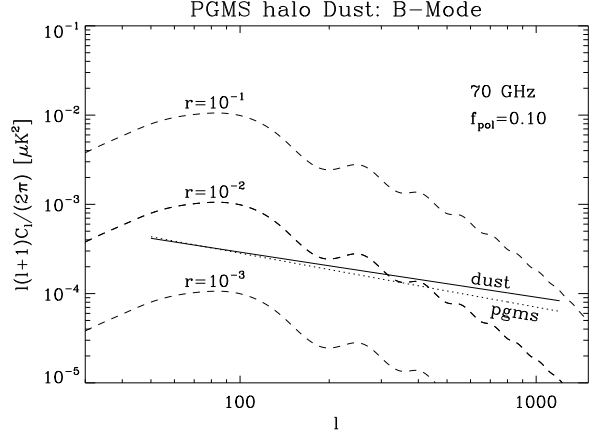


Figure 18. Estimates of the dust polarized emission in the halo section of the PGMS at 70 GHz (solid). The best fit to the temperature spectrum is used assuming a dust polarization fraction $f_{\text{pol}} = 0.10$ and then scaled to 70 GHz. The synchrotron emission spectrum estimated in Sect. 5 is shown for comparison, as well as the CMB B -Mode spectra for three different r values.

cent shift the frequency of minimum to 80GHz and 60GHz respectively.

This result is similar to that of the general high Galactic latitudes and suggests that the synchrotron-to-dust power ratio is only marginally dependant on the strength of the Galactic emission.

7 LIMITS ON r

To estimate the detection limits of r in the presence of the foreground contamination in the PGMS halo section, we consider an experiment with resolution of 1-degree at the CMB frequency channel to have adequate sensitivity at the $\ell \sim 90$ peak.

We also account for the cleaning provided by foreground separation techniques. We consider the two cases discussed by Tucci et al. (2005):

(i) cleaning by scaling the foreground map using just one frequency spectral index for all pixels. It is a coarse method and represents a worst case. The residual contamination depends on the spread of spectral indices in the area. We use $\Delta\alpha_s = 0.15$ for the synchrotron component, which is the value quoted for the high Galactic latitudes (Bernardi et al. 2004; Gold et al. 2009), and assume the same dispersion for the dust emission ($\Delta\alpha_d = 0.15$). We refer to this method as *clean #1*.

(ii) cleaning assuming knowledge of the frequency spectral index for any individual pixel. In this case the amplitude of the residual contamination depends on the measurement error of the frequency slopes. Here we assume a combination of the PGMS data with a *synchrotron channel* at 22 GHz onboard the CMB experiment with resolution of 1° and sufficient sensitivity to give $S/N = 5$. For the dust emission, we assume that the CMB experiment includes a *dust channel* at 350 GHz with a sensitivity to allow a $S/N = 5$ and resolution scaled from the CMB channel. We refer to this method as *clean #2*.

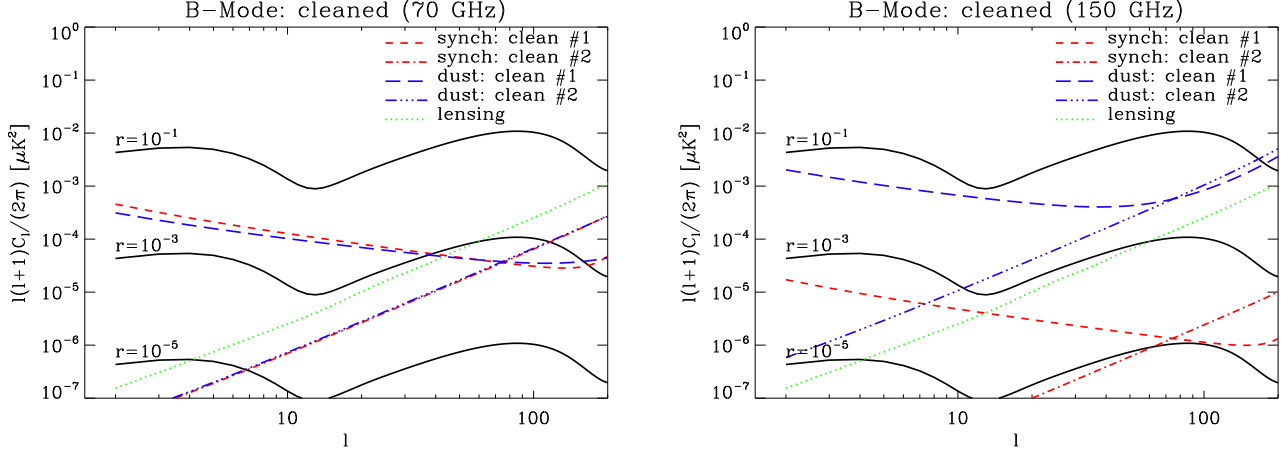


Figure 19. Residual contaminations in the PGMS halo section at 70 (left) and 150 GHz (right) for synchrotron (red) and dust emission (blue). Results for both the two cleaning methods described in text are shown. The gravitational lensing contribution is also shown assuming that cleaning has dimmed its amplitude by a factor 10 in spectrum (green).

Table 8. Detection limits of r at 3-sigma C.L. (δr) at 70 and 150 GHz in the PGMS halo area and in a 2500-deg² region assumed to have equivalent foreground contamination (see text). Results for both cleaning types described in the text are reported.

Area	clean type	δr (70 GHz)	δr (150 GHz)
PGMS	clean #1	2.2×10^{-3}	8.0×10^{-3}
PGMS	clean #2	1.5×10^{-3}	5.5×10^{-3}
2500-deg ²	clean #1	1.2×10^{-3}	4.2×10^{-3}
2500-deg ²	clean #2	0.5×10^{-3}	1.8×10^{-3}

These two methods are at the two ends of the cleaning capabilities (#1 is coarser and less efficient, #2 is finer and more efficient) so giving a good idea of the range of the possible performances.

The left panel of Figure 19 shows the residual contaminations left by these two methods at 70 GHz in the PGMS halo section using the method of Tucci et al. (2005). The effect of method #1 is to reduce the amplitude of the contamination but preserve the shape of the power spectrum (for instance, the synchrotron residual preserves the angular spectral index of -2.6). Method #2 gives comparable results at the 2° CMB peak, but has a flat white-noise-like spectrum which performs much better on large angular scales. Therefore, while the simpler clean #1 looks sufficient when the target of the CMB experiment is the peak at $\ell \sim 90$, the clean #2 is better suited for the reionization bump at larger scales.

With such low levels of residual contamination the effects of gravitational lensing become a dominant part of the foreground contamination budget, which would thus also need to be subtracted to exploit the low Galactic emission of the PGMS strip. Gravitational lensing effects can be cleaned using high resolution data (10 arcmin or better, Seljak & Hirata 2004) and here we assume that it can be reduced by 10 fold (in the spectrum).

The Fisher information matrix is used to estimate the detection limits (Tegmark, Taylor & Heavens 1997; Tegmark 1997). The Fisher matrix gives the inverse of the covariance matrix of the parameters to be estimated from

the data sample used, which, in our case, are the cosmological parameters and the angular power spectra, respectively.

We assume that r is the only parameter to be measured, with the other cosmological parameters provided by Temperature and E -Mode spectrum, also from other experiments like WMAP or the forthcoming PLANCK. Then the Fisher matrix reduces to the scalar

$$\mathcal{F}_{rr} = \sum_{\ell} \frac{1}{(\Delta C_{\ell}^B)^2} \left(\frac{\partial C_{\ell}^B}{\partial r} \right)^2 \quad (6)$$

and the error on r is $\sigma_r = \mathcal{F}_{rr}^{-1/2}$. The uncertainty ΔC_{ℓ}^B of the B -mode spectrum in the case of sky fraction coverage f_{sky} is a function of the CMB spectrum $C_{\ell}^{B,\text{cmb}}$ and the cleaning residuals of synchrotron, dust, and gravitational lensing:

$$\Delta C_{\ell}^B = \sqrt{\frac{2}{(2\ell+1)L f_{\text{sky}}}} C_{\ell}^{B,\text{cmb}} + (C_{\ell}^{B,\text{synch-res}} + C_{\ell}^{B,\text{dust-res}} + C_{\ell}^{B,\text{lens-res}}), \quad (7)$$

where L is the size of the multipole bands. The instrumental noise is not present here since we only want to investigate the detection limits due to foregrounds. As a set of cosmological parameters we use the best fits of the 5-yr WMAP data release (Komatsu et al. 2009).

At 70 GHz the detection limits of r in the PGMS halo region is $\delta r \sim 2 \times 10^{-3}$ (3-sigma C.L.) for both the two cleaning methods (Tab. 8). This is a very low level which makes the PGMS strip an excellent target for CMB experiments

and enables accessing levels of r much lower than previously estimated for areas of comparable size (e.g. Tucci et al. 2005; Verde et al. 2006, who used higher foreground levels estimated from total intensity data). An important consideration is that there is only a marginal benefit from using the more sophisticated cleaning method. For a 250-deg² area most of the sensitivity resides in the $\ell \sim 90$ peak, where the dominant residual is the gravitational lensing and a better cleaning of the other contaminants is not justified.

This result is therefore quite robust since it is based both on actual measurements of the foreground contamination in a specific area and on the use of a coarse cleaning method. Moreover, the leading residual term is the gravitational lensing, giving a good margin against errors of our dust polarization fraction assumption.

This result provides a sound basis for investigating the B -Mode. The detection limit we have found here is even better than the goals of the most advanced ground-based experiments and proves that there exists at least one area of the sky where it is realistic to carry out investigations of the B -mode down to very low limits of r .

It is also important to estimate δr for 150 GHz, a frequency that, although far from the foreground minimum, is preferred by experiments based on bolometric detectors. This frequency is chosen for both excellent sensitivities of the sensors and for the more compact size allowed. As shown in Figure 19, right panel, the leading residual at this frequency is the dust. Although this increases the detection limit to $\delta r = 6\text{--}8 \times 10^{-3}$ (Tab. 8), it is better than the goals of the most advanced sub-orbital experiments planned for the next years, typically set to $r \sim 1 \times 10^{-2}$ (e.g. CLOVER, SPIDER, EBEX, North et al. 2008; Crill et al. 2008; Grainger et al. 2008).

This can have relevant impact on CMB experiment designs. If the detection level is limited to $r = 1 \times 10^{-2}$ by the instrument sensitivity the experiment can be designed to use 150 GHz as *CMB-channel*, with clear advantages of detector sensitivity (bolometric detectors are the most sensitive, currently) and instrument size. Moreover, low frequency channels dedicated to measuring the synchrotron emission would not be needed because this foreground would be so faint at 150 GHz to not need cleaning.

Alternatively, if the goal is to devise an experiment to reach the best possible r detection limit constrained only by foregrounds, the best frequency is 70 GHz, which enables limits four-fold better than at 150 GHz.

The PGMS halo region is a narrow strip 50° long and it is unlikely that its optimal conditions are confined to its 5° width. Therefore we consider now a larger area of 50° × 50°, an area equally extended in both directions. This area, about 6% of the sky, is chosen to match the southern portion of the low emission region identified in the WMAP data (Carretti et al. 2006b).

The detection limits achievable over such an area are further reduced over those possible from the PGMS halo section alone, and reach $\delta r = 5 \times 10^{-4}$ (3-sigma C.L.) if method #2 is applied, or $\delta r = 1.2 \times 10^{-3}$ under the application of the coarser method #1 (Tab. 8). These r values are very low and compare to the goals of the space missions under study such as B-POL and CMBPol (de Bernardis et al. 2008; Baumann et al. 2008). Such an area is sufficiently compact to be observable by a ground-based or a balloon-borne

experiment, and so might suggest a change of strategy for detecting the CMB B -Mode. Values of r thought detectable only with space experiments could be reachable with easier and cheaper sub-orbital programmes, leaving the space option only for the ultimate limits ($r \sim 10^{-5}$) achievable only with a very large sky fraction.

Note that in this case there is a significant difference between the two cleaning methods, justifying the use of the more sophisticated method #2. This is because the larger area makes measurement of the lowest multipole components meaningful, where method #1 is not effective in removing the Galactic foregrounds, whereas the more efficient method #2 is only limited by gravitational lensing effects.

8 SUMMARY AND CONCLUSIONS

The PGMS has mapped the radio polarized emission at all Galactic latitudes in a 5 degree strip at a frequency sufficiently high not to be affected by Faraday depolarization and with sufficient sensitivity to detect the signal in low emission regions. It is the largest area observed so far at high Galactic latitude uncontaminated by large local structures.

This has enabled us to investigate the behaviour of the polarized emission with latitude by computing the polarized angular power spectrum in 17 fields from the Galactic plane to the South Galactic pole. We can distinguish three latitude sections: two main regions well distinguished by both brightness and structure of the emission (disc and halo), and an extended transition connecting them. In detail they are:

1. The halo at high Galactic latitudes ($b = [-90^\circ, -40^\circ]$) featured by low emission fields with steep spectra (angular slope $\beta = [-3.0, -2.0]$), that is smooth emission dominated by large scale structures. The slope is almost uniformly distributed within a wide range, with median $\beta_{\text{med}}^{EB} = -2.6$ and dispersion $\sigma_{\beta^{EB}} = 0.24$. No clear variation of either slope or amplitude with Galactic latitude is apparent because of the large field-to-field fluctuations. A trend of increasing emission toward lower latitudes might be present, but if it exists, is a minor term.

2. A transition region at mid-latitudes ($b = [-40^\circ, -20^\circ]$) whose angular spectra are steep like those of the halo, but shows an increase of the emission power with decreasing latitude.

3. The disc at low latitudes ($b = [-20^\circ, 0^\circ]$) characterized by inverted spectra with slopes in a narrow range of mean $\beta^{EB} = -1.8$ and dispersion $\sigma_{\beta^{EB}} = 0.08$. The emission is mostly uniformly distributed across the angular scales with a slight predominance of the small ones. The amplitudes are two orders of magnitude brighter than in the halo and the power gradually increases towards the Galactic plane.

The change in the angular slope around $b = -20^\circ$ is quite sudden and identifies a sharp disc-halo transition from the smooth emission of the mid-high latitudes to the more complex behaviour of the disc; this is likely related to the more turbulent and complex structure of the ISM.

The halo section has no clear trend with the latitude of either emission power or angular slope. The high Galactic latitudes above 40° are thus just one environment, at least

in the low emission region not contaminated by local anomalies the PGMS intersects. This is very important for CMB investigations, as it indicates that it is possible to find large areas with optimal conditions for seeking the *B*-Mode: the halo section of the PGMS strip has a 50° extent, at least along one dimension.

The synchrotron emission of the whole PGMS halo section is very weak. Once scaled to 70 GHz it is equivalent to $r = 3.3 \times 10^{-3}$, which could even not require any cleaning if an experiment aims at a detection limit of $r = 0.01$ – 0.02 .

The dust component is also faint and equal to the synchrotron emission at 60–80 GHz for polarization fractions between 5 and 20 %. The frequency of minimum foreground in this low emission region is thus similar to that found with WMAP for the general high Galactic latitudes (75% of the sky). If confirmed in other regions, this would imply both that the dust-synchrotron power ratio is rather independent of the brightness of the Galactic emission and the frequency of minimum foreground nearly independent of the sky position.

We estimate the r detection limit of this area accounting for the use of foreground cleaning procedures. We apply both a coarse and a more refined method. The Galactic emission is so low that the dominant residual contamination is the gravitational lensing even assuming to clean it by 10 folds. For both the two cleaning methods the detection limit is $\delta r \sim 2 \times 10^{-3}$ (3-sigma C.L.) if the CMB *B*-Mode search is conducted at 70 GHz, and $\delta r \sim 7 \times 10^{-3}$ at 150 GHz. The former is very appealing, but already the latter is better than the detection limits aimed by the most advanced sub-orbital experiments planned for the next years, usually set to $\delta r = 0.01$.

These results are valid in the area actually observed by our survey. However, the PGMS halo section is extended over 50° along one dimension and it is unlikely that its excellent conditions are confined to its 5° width. We have thus analysed the case of a larger area assuming that it can have equal extension along the other dimension. This is not fully arbitrary since its size (6% of the sky) matches the southern portion of the best area of the sky. In such a $50^\circ \times 50^\circ$ region the r detection limit drops to $\delta r = 5 \times 10^{-4}$ (3-sigma) at 70 GHz, which is comparable with the goals of the space missions currently under study, but with the non-trivial advantage that such an area is still sufficiently compact to be observable by a sub-orbital experiment. The results obtained here might suggest a review of plans to detecting the CMB *B*-Mode and associated investigations of the inflationary scenarios.

While the detection limit is limited to $\delta r = 1 \times 10^{-2}$ by the detector array size and sensitivity, observations at 150 GHz are sufficient if conducted in the PGMS area (or one with equivalent foreground properties) with clear advantages of using the currently best detectors (bolometers) and of an experiment more compact than at 70 GHz. Moreover, the synchrotron emission we have detected in this area is sufficiently weak at 150 GHz not to require any cleaning, which removes the need for low frequency channels to measure it. An initial *exploratory* class of observation could be conducted with a compact equipment over an area for which the foreground conditions have been verified to be sufficiently low. Experiments like EBEX or CIOVER already belong to this class, not only because of the design choices,

but also because their target areas intersect the PGMS strip (Grainger et al. 2008; North et al. 2008).

A deeper detection limit, down to $\delta r = 2 \times 10^{-3}$, could be reached by a suborbital experiment observing the same area but with the *CMB channel* shifted to 70 GHz. The inclusion of a channel at a lower frequency would be required to measure the synchrotron component.

A final step of suborbital experiments could reach down to $\delta r = 5 \times 10^{-4}$ observing at 70 GHz in a large area of $50^\circ \times 50^\circ$ having the PGMS foreground levels. The location of the most suitable region must be determined, a task that can be accomplished by the forthcoming large foreground surveys like the S-band Polarization All Sky Survey (S-PASS), or the C-band All Sky Survey (C-BASS).

It is worth noticing that the gravitational lensing needs to be cleaned to actually take advantage of the low Galactic emission of the PGMS halo section. This can be effectively carried out only with high resolution data ($10'$ or finer, Seljak & Hirata 2004) and the design of CMB experiments should comply with that rather than be limited to 1-degree to fit the peak at $\ell \sim 90$.

The limit $r \sim 1 \times 10^{-3}$ is an important threshold for the inflationary physics since it is about the lower limit of the important class of inflationary models with low degree of fine tuning (Boyle et al. 2006). Our study shows that this threshold can be reached with an easier and cheaper sub-orbital experiment rather than a more complex space mission, making this goal more realistically achievable with a smaller budget and in a shorter time than that required to develop space-borne equipment.

A space mission could be the last step aimed at reaching the lowest limits allowed by the CMB *B*-Mode (of the order of $r = 10^{-5}$, Amarie et al. 2005), or measuring r with the highest possible accuracy if already detected in one of the former steps. This can be obtained only by observing most of the sky, both to measure the largest scales and to minimise the cosmic variance, an experiment that can only be accomplished from space.

The PGMS data will be made available at the site <http://www.atnf.csiro.au/people/Ettore.Carretti/PGMS>

ACKNOWLEDGMENTS

This work has been partly supported by the project SPORt funded by the Italian Space Agency (ASI) and by the ASI contract I/016/07/0 *COFIS*. We wish to thank Warwick Wilson for his support in the DFB1 set-up, and John Reynolds for the observations set-up. Part of this work is based on observations taken with the Parkes Radio Telescope, which is part of the Australia Telescope, funded by the Commonwealth of Australia for operation as a National Facility managed by CSIRO. We acknowledge the use of the CMBFAST and HEALPix packages.

REFERENCES

- Amarie M., Hirata C., Seljak U., 2005, PRD, 72, 123006
- Baumann D., et al., 2008, arXiv:0811.3911 [astro-ph]

- Beck R., 2008, in "The UV Window to the Universe", eds. A.I. Gomez de Castro and M. Castellanos, Ap&SS, in press, arXiv:0711.4700 [astro-ph]
- Benoît A., et al., 2004, A&A, 424, 571
- Bernardi G., Carretti E., Fabbri R., Sbarra C., Poppi S., Cortiglioni S., Jonas J.L., 2004, MNRAS, 351, 436
- Bernardi G., Carretti E., Sault R.J., Cortiglioni S., Poppi S., 2006, MNRAS, 370, 2064
- Boyle L.A., Steinhardt P.J., & Turok N., 2006, Phys. Rev. Lett. 96, 111301
- Brown J.C., Haverkorn M., Gaensler B.M., Taylor A.R., Bizunok N.S., McClure-Griffiths N.M., Dickey J.M., Green A.J., 2007, ApJ, 663, 258
- Carretti E., Bernardi G., Sault R.J., Cortiglioni S., & Poppi S., 2005a, MNRAS, 358, 1
- Carretti E., McConnell D., McClure-Griffiths N.M., Bernardi G., Cortiglioni S., & Poppi S., 2005b, MNRAS, 360, L10
- Carretti E., Poppi S., Reich W., Reich P., Fürst E., Bernardi G., Cortiglioni S., Sbarra C., 2006a, MNRAS, 367, 132
- Carretti E., Bernardi G., Cortiglioni S., 2006b, MNRAS, 373, L93
- Crill B.P., et al., 2008, in Space Telescopes and Instrumentation 2008: Optical, Infrared, and Millimeter, Eds. J.M. Oschmann Jr., M.W.M. de Graauw & H.A. MacEwens, Proc. of SPIE, 7010, 70102P
- de Bernardis P., Bucher M., Burigana C., Piccirillo L., 2008, Exp. Astron., in press, arXiv:0808.1881 [astro-ph]
- Emerson D.T., Gräve R., 1988, A&A, 190, 353
- Finkbeiner D.P., Davis M., Schlegel D.J., 1999, ApJ, 524, 867
- Gold B., et al., 2009, ApJS, in press, arXiv:0803.0715 [astro-ph]
- Górski K.M., et al., 2005, ApJ, 622, 759
- Grainger W., et al., 2008, in Millimeter and Submillimeter Detectors and Instrumentation for Astronomy IV, Eds. W.D. Duncan, W.S. Holland, S. Withington, J. Zmuidzinas, Proc. of SPIE Vol. 7020 70202N-2
- Han J.L., 2002, in Astrophysical Polarized Backgrounds, eds. S. Cecchini, S. Cortiglioni, R. J. Sault, C. Sbarra, AIP Conf. Ser., 609, 96
- Han J.L., Manchester R.N., Lyne A.G., Qiao G.J., van Straten W., 2006, ApJ, 642, 868
- Haverkorn, M., Gaensler B.M., McClure-Griffiths N.M., Dickey, J.M., Green A.J., 2006, ApJS, 167, 230
- Kamionkowski M., Kosowsky A., 1998, PRD, 57, 685
- Komatsu E., et al., 2009, ApJS, in press, arXiv:0803.0547 [astro-ph]
- Lange A., 2008, in CMB component separation and the physics of foregrounds, http://planck.ipac.caltech.edu/content/ForegroundsConference/presentationsForWEB/58_andrewLange.pdf
- La Porta L., Burigana C., Reich W., Reich P., 2006, A&A, 455, L9
- Masi S., et al., 2006, A&A, 458, 687
- North C.E., et al., 2008, in XXXXIII Rencontres de Moriond "Cosmology", in press, arXiv:0805.3690 [astro-ph]
- Page L., et al., 2007, ApJS, 170, 335
- Pryke C., et al., 2008, ApJ, submitted, arXiv:0805.1944 [astro-ph]
- Reynolds J.E. 1994, ATNF Tech. Doc. Ser. 39.3040
- Sbarra C., Carretti E., Cortiglioni S., Zannoni M., Fabbri R., Macculi C., Tucci M., 2003, A&A, 401, 1215
- Seljak U., Hirata C.M., 2004, PRD, 69, 043005
- Sun X.H., Reich W., Waelkens A., Enßlin T.A., 2008, A&A, 477, 573
- Takahashi Y.D., et al., 2008, in Millimeter and Submillimeter Detectors and Instrumentation for Astronomy IV, Eds. W.D. Duncan, W.S. Holland, S. Withington, J. Zmuidzinas, Proc. of SPIE, 7020, 70201D
- Tegmark M., 1997, PRD, 56, 4514
- Tegmark M., Taylor A.N., Heavens A.F., 1997, ApJ, 480, 22
- Testori J.C., Reich P., Reich W., 2008, A&A, 484, 733
- Tucci M., Martínez-González E., Vielva P., Delabrouille J., 2005, MNRAS, 360, 935
- Verde L., Peiris H.V., Jimenez R., 2006, JCAP, 1, 19
- Wolleben M., Landecker T.L., Reich W., Wielebinski R., 2006, A&A, 448, 411
- Zaldarriaga M., 1998, Ph.D. Thesis, M.I.T., astro-ph/9806122

This paper has been typeset from a \LaTeX file prepared by the author.